SANDIA REPORT

SAND2021-1752
Printed February 2021

Sandia National Laboratories

Thermal-Mechanical Elastic-Plastic and Ductile Failure Model Calibrations for 304L Stainless Steel Alloy

E. Corona, S.L.B. Kramer, B.T. Lester, A.R. Jones, B. Sanborn, L. Shand and C.J. Fietek

Prepared by
Sandia National Laboratories
Albuquerque, New Mexico 87185
Livermore, California 94550

Issued by Sandia National Laboratories, operated for the United States Department of Energy by National Technology & Engineering Solutions of Sandia, LLC.

Available to DOE and DOE contractors from

U.S. Department of Energy
Office of Scientific and Technical Information
P.O. Box 62
Oak Ridge, TN 37831

Telephone: (865) 576-8401
Facsimile: (865) 576-5728
E-Mail: reports@osti.gov
Online ordering: http://www.osti.gov/scitech

Available to the public from

U.S. Department of Commerce
National Technical Information Service
5301 Shawnee Road
Alexandria, VA 22312

Telephone: (800) 553-6847
Facsimile: (703) 605-6900
E-Mail: orders@ntis.gov
Online order: https://classic.ntis.gov/help/order-methods

ABSTRACT

Numerical simulations of metallic structures undergoing rapid loading into the plastic range require material models that accurately represent the response. In general, the material response can be seen as having four interrelated parts: the baseline response under slow loading, the effect of strain rate, the conversion of plastic work into heat and the effect of temperature. In essence, the material behaves in a thermal-mechanical manner if the loading is fast enough so when heat is generated by plastic deformation it raises the temperature and therefore influences the mechanical response. In these cases, appropriate models that can capture the aspects listed above are necessary. The material of interest here is 304L stainless steel, and the objective of this work is to calibrate thermal-mechanical models: one for the constitutive behavior and another for failure.

The work was accomplished by first designing and conducting a material test program to provide data for the calibration of the models. The test program included uniaxial tension tests conducted at room temperature, 150 and 300°C and at strain rates between 10^{-4} and 10^{3} 1/s. It also included notched tension and shear-dominated compression hat tests specifically designed to calibrate the failure model. All test specimens were extracted from a single piece of plate to maintain consistency. The constitutive model adopted was a modular J_2 plasticity model with isotropic hardening that included rate and temperature dependence. A criterion for failure initiation based on a critical value of equivalent plastic strain fitted the failure data appropriately and was adopted.

Possible ranges of the values of the parameters of the models were determined partially on historical data from calibrations of the same alloy from other lots and are given here. The calibration of the parameters of the models were based on finite element simulations of the various material tests using relatively fine meshes and hexahedral elements. When using the model in structural finite element calculations, however, element formulations and sizes different from those in the calibration are likely to be used. A brief investigation demonstrated that the failure initiation predictions can be particularly sensitive to the element selection and provided an initial guide to compensate for the effect of element size in a specific example.

ACKNOWLEDGMENT

This work was made possible by the work of the staff members in the Structural Mechanics and the Experimental Impact Mechanics Laboratories as well as of Jack Heister, Product Design Engineer. We also acknowledge the technical inputs by Bill Scherzinger and Adam Brink during the course of this work. Special thanks go to Doug VanGoethem and Kyle Karlson for reviewing the document and providing thoughtful comments that have improved the report.

Sandia National Laboratories is a multimission laboratory managed and operated by National Technology & Engineering Solutions of Sandia, LLC, a wholly owned subsidiary of Honeywell International Inc., for the U.S. Department of Energy's National Nuclear Security Administration under contract DE-NA0003525.

CONTENTS

LIST OF FIGURES

LIST OF TABLES

NOMENCLATURE

A	Power-law hardening constant
A_n	Cross-sectional area of notch
C	Johnson-Cook strain rate parameter
D	Damage parameter in ductile failure model
F	Force
K	Element-size-dependent value of D at failure
L_g	Extensometer gage length
R	Cross-sectional radius of notch
T	Temperature
T_o	Initial temperature
W^p	Plastic work
c_p	Specific heat capacity
l	Element size
n	Power-law exponent
r	Notch radius
t	Time
Δ	Machine stroke or global displacement
δ	Displacement between points on a specimen
ε	Engineering uniaxial strain
$\dot{\varepsilon}$	Engineering uniaxial strain rate
$\dot{\varepsilon}_o$	Reference strain rate in Johnson Cook rate dependence
$\bar{\varepsilon}^p$	True equivalent plastic strain
ρ	Density
σ	Engineering uniaxial stress
$\bar{\sigma}$	True equivalent stress
θ	Temperature
θ_L	Lode angle
σ_t	True stress
σ_y	Power-law yield stress

1. INTRODUCTION

Applications in which significant loads are quickly applied to metallic structures to cause rapid plastic deformations and possibly ductile failure require the use of calibrated thermal-mechanical constitutive and failure models. The objective of the work presented here is to calibrate relatively simple, appropriate models for 304L stainless steel that address its elastic-plastic response and the initiation of failure. The models are part of the modular plasticity and failure model implementations in Sierra/SM [1] with capabilities to address adiabatic heating and the effects of temperature and strain rate in the response of the material.

Calibrating phenomenological material models, such as the ones used here, requires test data. The range of applicability of the calibrations in terms of temperature, strain rate and, in the case of the failure model, the states of stress sampled, depends on the breadth of the test data available. For the current calibration, a systematic test program was designed to provide data for loading environments with strain rates of up to 10^3 1/s. Most of the values of the model parameters were then adjusted based on the results of finite element simulations of the tests. Once completed, the predictions by the calibrated models in structural finite element models may depend on the element type and size used (these will likely be different from the ones used in calibration), especially when related to the analysis of ductile failure.

The mechanical behavior of stainless steel 304L exhibits some particular characteristics that the calibrated model must address and the calibration process contend with. Among those are: large ductility, significant strain rate sensitivity even at room temperature and sensitivity of the stress-strain curve shape to moderate changes in temperature. Other interesting details of the response, such as dynamic strain aging that shows up as serrated uniaxial stress-strain curves at some combinations of strain rate and temperature cannot be captured by the model and are therefore neglected. Another important aspect of this material relates to its perhaps above average variations in lot-to-lot mechanical properties. Therefore, establishing possible ranges for the variability of the model's parameters should be considered in applications where it may be consequential.

1.1. Material Description

Austenitic stainless steel, of which the alloy 304L is a type, is the family of stainless steel with the largest production [2]. The crystal structure is face-centered cubic and is designed to remain the same from cryogenic temperatures to the melting point. Since they possess the same microstructure at all temperatures, they are not hardenable by heat treatment. Stainless steels in general are iron-based alloys that are resistant to oxide corrosion because of a significant amount of chromium present. Another major element in austenitic stainless steels is nickel, which is used

to achieve the austenitic microstructure. The 304 alloy contains 18-20% chromium and 8-12% nickel. The "L" in 304L indicates that it is a low-carbon alloy, with under 0.03% carbon. Typical ranges in the composition of 304L alloy are given in Table 1-1.

Table 1-1. Typical composition of 304L stainless steel (weight %) [3]

Cr	Ni	C	Mn	P	S	Si	Fe
18–20	8–12	Max. 0.03	Max. 2	Max. 0.045	Max. 0.03	Max. 1	Balance

The focus of the work presented here is in the mechanical response of 304L stainless steel from a stress-free state to failure, at temperatures in the vicinity of room temperature and loading rates that are consistent with environments that generate strain rates in the range of 10^3 1/s or lower. At these rates of loading, the temperature in the material may increase due to the dissipative nature of plastic work, so the effects of high temperatures, up to a few hundred degrees Celsius, also need to be accounted for.

The material stock used for the model calibration consisted of 1-inch plate that was shared to make specimens related to other structural testing needs. The material was purchased through Superior Machine Co. in February of 2018. The material that was delivered consisted of 5 plates: Two plates were 48 in. $\times$ 240 in. from a single heat, two others were 60 in. $\times$ 240 in. from a different, single heat while the third was 48 in. $\times$ 144 in. from yet a third heat, as shown in the certs in Fig. 1-1. These facts were not discovered until later in the program when the uniaxial tension test engineering stress-strain curves from two test series conducted in 2019 [4] and 2020 showed noticeable differences as can be seen in Fig. 1-2. The suspicion is that these curves came from different plate heats, but concrete proof is not available. The material calibrations in this report all come from a single plate that corresponds to the 2020 test in Fig. 1-2.

The mechanical behavior of 304L stainless steel could be briefly described as follows. The material has a relatively low proportional limit compared to the yield stress, so the linearly elastic regime is comparatively small with respect to many other steel alloys. The material hardens significantly during plastic deformation and therefore the ultimate stress, or tensile strength, is significantly larger than the yield stress, as can be appreciated in Fig. 1-2. This material is sensitive to the rate of loading and exhibits significant creep and relaxation, even at room temperature, when compared to other steel alloys. In addition, the response of the material is significantly affected by temperature. The material is significantly ductile, achieving elongations at failure from its virgin state that are larger than 60% as can again be seen in Fig. 1-2. Therefore, in order to capture the mechanical behavior of this material at large deformations its thermal-mechanical response needs to be addressed and modeled, especially when the environment includes loading under which the response of the material cannot be taken as isothermal.

1.2. Intended Use

The intended use of the calibrated material model for 304L stainless steel presented here is in structural simulations where the loading takes the material into the plastic range and where the

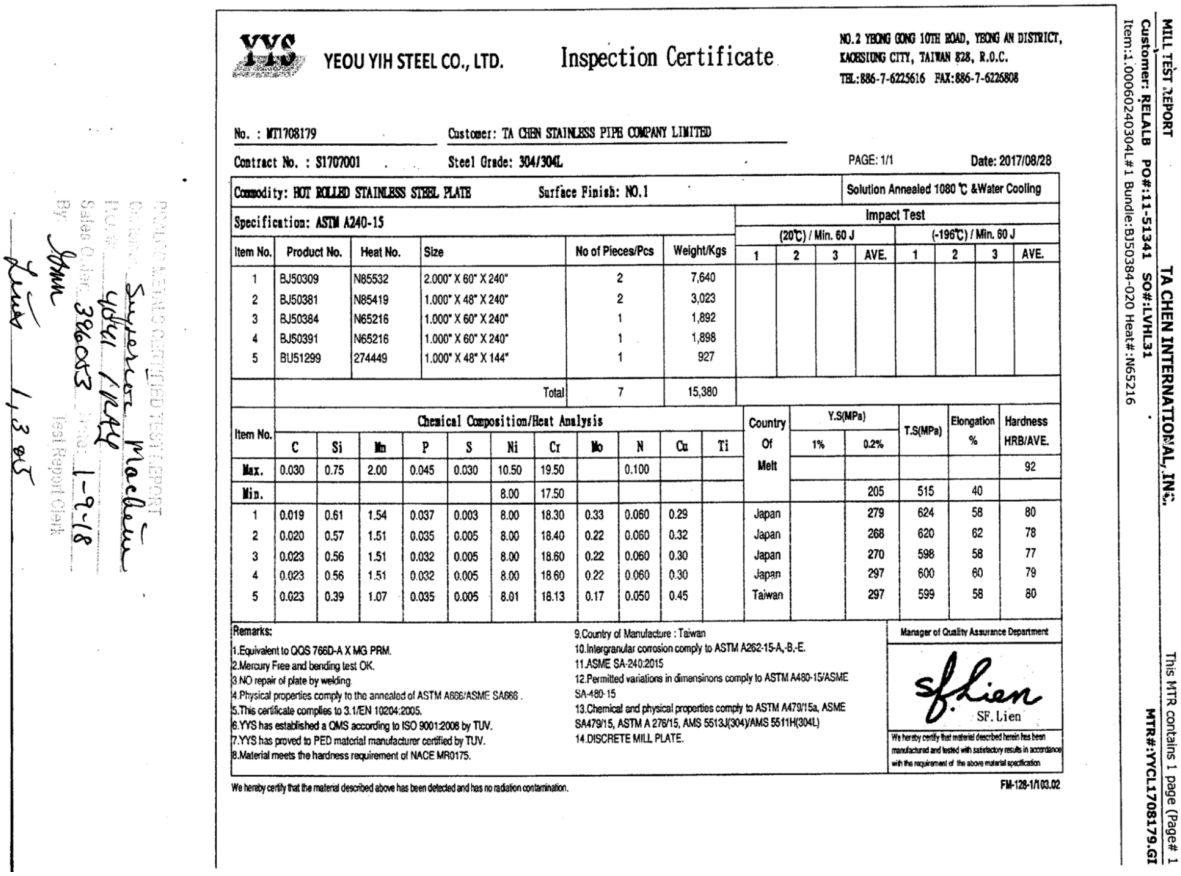

YEOU YIH STEEL CO., LTD.

Inspection Certificate

NO.2 YEONG GONG 10TH ROAD, YEONG AN DISTRICT, KAOHSIUNG CITY, TAIWAN 828, R.O.C.
TEL:886-7-6225616 FAX:886-7-6226808

No. : MT1708179 Customer: TA CHEN STAINLESS PIPE COMPANY LIMITED
Contract No. : S1707001 Steel Grade: 304/304L PAGE: 1/1 Date: 2017/08/28

Commodity: HOT ROLLED STAINLESS STEEL PLATE Surface Finish: NO.1 Solution Annealed 1080 ℃ &Water Cooling

Specification: ASTM A240-15

Item No.	Product No.	Heat No.	Size	No of Pieces/Pcs	Weight/Kgs	Impact Test (20℃) / Min. 60 J 1	2	3	AVE.	(-196℃) / Min. 60 J 1	2	3	AVE.
1	BJ50309	N85532	2.000" X 60" X 240"	2	7,640								
2	BJ50381	N85419	1.000" X 48" X 240"	2	3,023								
3	BJ50384	N65216	1.000" X 60" X 240"	1	1,892								
4	BJ50391	N65216	1.000" X 60" X 240"	1	1,898								
5	BU51299	274449	1.000" X 48" X 144"	1	927								
			Total	7	15,380								

Item No.	Chemical Composition/Heat Analysis C	Si	Mn	P	S	Ni	Cr	Mo	N	Cu	Ti	Country Of Melt	Y.S(MPa) 1%	0.2%	T.S(MPa)	Elongation %	Hardness HRB/AVE.
Max.	0.030	0.75	2.00	0.045	0.030	10.50	19.50		0.100								92
Min.						8.00	17.50							205	515	40	
1	0.019	0.61	1.54	0.037	0.003	8.00	18.30	0.33	0.060	0.29		Japan		279	624	58	80
2	0.020	0.57	1.51	0.035	0.005	8.00	18.40	0.22	0.060	0.32		Japan		268	620	62	78
3	0.023	0.56	1.51	0.032	0.005	8.00	18.60	0.22	0.060	0.30		Japan		270	598	58	77
4	0.023	0.56	1.51	0.032	0.005	8.00	18.60	0.22	0.060	0.30		Japan		297	600	60	79
5	0.023	0.39	1.07	0.035	0.005	8.01	18.13	0.17	0.050	0.45		Taiwan		297	599	58	80

Remarks:
1.Equivalent to OQS 766D-A X MG PRM.
2.Mercury Free and bending test OK.
3.NO repair of plate by welding.
4.Physical properties comply to the annealed of ASTM A666/ASME SA666 .
5.This certificate complies to 3.1/EN 10204:2005.
6.YYS has established a QMS according to ISO 9001:2008 by TUV.
7.YYS has proved to PED material manufacturer certified by TUV.
8.Material meets the hardness requirement of NACE MR0175.
9.Country of Manufacture : Taiwan
10.Intergranular corrosion comply to ASTM A262-15-A,-B,-E.
11.ASME SA-240:2015
12.Permitted variations in dimensions comply to ASTM A480-15/ASME SA-480-15
13.Chemical and physical properties comply to ASTM A479/15a, ASME SA479/15, ASTM A 276/15, AMS 5513J(304)/AMS 5511H(304L)
14.DISCRETE MILL PLATE.

Manager of Quality Assurance Department
SF. Lien
We hereby certify that material described herein has been manufactured and tested with satisfactory results in accordance with the requirement of the above material specification

We hereby certify that the material described above has been detected and has no radiation contamination.

FM-126-1/1.03.02

MILL TEST REPORT TA CHEN INTERNATIONAL,INC. This MTR contains 1 page (Page# 1
Customer: RELALB PO#:11-51341 SO#:LVHL31 MTR#:YYCL1708179.GI
Item:1.000602403O4L# 1 Bundle:BJ50384-020 Heat#:N65216

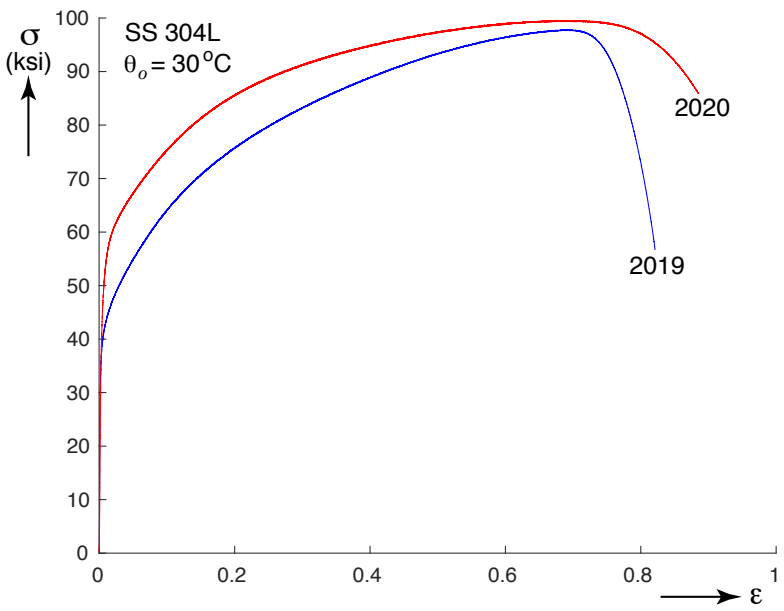

Figure 1-2. Comparison of uniaxial tension test engineering stress-strain curves from 304L stainless steel plates tested in 2019 and 2020.

possibility of failure needs to be investigated. As a result, the constitutive model considered here accounts for the effects of temperature up to 300°C and strain rates up to 10^3 1/s. This model is then complemented with a ductile failure model that accounts for the dependence of failure on the loading history, plus rate and temperature effects.

The calibration procedures used here involve simulations of material tests where the specimens are modeled using finite elements with relatively small selective deviatoric hexahedral elements. Given that structural applications may utilize elements that are of different size and type such as shell elements, the calibrations, especially of the failure model, need to be interpreted accordingly to better capture the desired structural behavior. Although the use of the model in a variety of applications under different loadings may be extensive, this report provides guidance based on relatively few, simple test geometries. While this guidance may suffice in some cases, it is important for analysts to exercise caution when using the model and consult with the calibration team when in doubt.

2. EXPERIMENTAL DATA

2.1. Design of Test Program

Time and equipment constraints dictated that the test program be designed to utilize the resources of the Structural Mechanics Laboratory (SML) and of the Experimental Impact Mechanics Laboratory (EIML) in Building 860 as efficiently as possible while subjecting the material samples to the environments of interest for the intended use of the models. An important component of the test design was therefore to minimize the number of specimen designs and test set-ups required. This led to a test program where all standard-sized tensile specimens would have a common gripping scheme and the sub-size specimens used for high strain rates could be tested either in a Kolsky bar in the EIML or in a standard testing machine in the SML. It was also decided to use test fixtures that were already available in the laboratory and measurement methods that had been well-developed whenever possible. The following sections describe each of the specimens used in the test program.

2.2. Specimen Designs and Test Set-ups

Four specimen designs were created for model calibration purposes that explore different aspects of the material response, and that give data that can be addressed in a logical sequence during the calibration procedure. The specimen designs can be briefly described as follows:

Standard-size uniaxial tension specimens: The principal purpose of these specimens was to obtain engineering stress-strain curves of the material at different temperatures ranging from 30 to 300°C at the slowest rate of loading. Tests were also conducted at a faster loading rate to explore rate dependence with different initial temperatures.

Sub-size uniaxial tension specimens: The purpose of these specimens was to obtain material response data from high-strain-rate uniaxial tension test specimens. These specimens were tested in the tensile Kolsky bar and the“Dropkinson” bar intermediate strain rate set-up in the EIML, and in the standard servo-hydraulic machines in the SML.

While the previous specimens provided data for both the plasticity and failure calibrations, the next two were used primarily for calibration of the failure model under slow loading, so the tests could be considered isothermal at room temperature. The response of these specimens can also be used as a validation test for the constitutive model calibration and even to make some final adjustments to the same.

Notched tension specimens: These specimens were used to generate data to address failure under tensile-dominated loading or, equivalently, under high hydrostatic mean stresses at low rates of loading.

Hat compression, shear-dominated specimen: This specimen provided failure data for shear-dominated states of stress at low rates of loading.

The next few sections describe the specimen designs for each case in detail in conjunction with the test set-ups. All specimens were cut from a single piece of one-inch plate of approximate size 12 in. by 12 in.

2.2.1. Standard-Size Uniaxial Tension Specimens for Thermal-Mechanical Tests

The traditional tension test provided the foundation for calibrating the basic elastic-plastic response of the material. An important requirement for these tests was that they provide data not just at room temperature, but also at 150 and 300°C to enable calibration of thermal-mechanical models. Figure 2-1 shows the specimen design, while Fig. 2-2 shows photographs of the test set-up. The principal objective of the design was for the specimen and grips to be relatively compact to fit in a thermal chamber and to have a small thermal mass in order to allow faster test turn-arounds.

In order to achieve a compact set-up, the threaded grips shown in Fig. 2-2(b) were used. Note that the grips attach to the load-train of the 22 kip test machine using pinned connections to allow quick installation of the specimen and minimize the effects of misalignments in the load train. A cooling system, not shown in the figures, was used just outside the chamber to reduce the thermal load in the testing machine components outside the thermal chamber.

The specimen in Fig. 2-1 consisted of a test section of circular cross-section with nominal diameter of 0.25 in. and length of 0.75 in. The diameter of the test section was slightly tapered from the ends towards the center as shown to drive failure to the mid-span. Since 304L stainless steel strain hardens considerably, the diameter of the specimen outside of the test section needed to be sufficiently large to prevent yielding. Both ends of the specimen had 5/8-18 threads to fit in the grips. In this specimen the ratio of the cross-sectional area of the threaded section to that of the test section is 6:1. The test section is sufficiently long to accommodate a high-temperature extensometer, rated at 300°C, with an initial gage length of 0.5 in. Other instrumentation in the set-up included a 25 kip load cell outside the thermal chamber, temperature sensors in the chamber and attached to the lower grip and a linear variable differential transformer (LVDT) to measure the machine actuator stroke that provided the feedback signal to control the applied tensile displacement.

The tensile tests were conducted at three temperatures, 30, 150 and 300°C, and two displacement rates, 0.25×10^{-3} and 0.075 in/s. These correspond to nominal strain rates of 3.33×10^{-4} and 0.1 1/s, respectively. All sensor outputs were digitally recorded with a frequency of 4 samples per second for the slow tests and 1000 samples per second for the fast tests. Typical durations for the tensile loading of the tests were 40 minutes for the slower tests and 6 seconds for the faster tests at

room temperature. The tests at higher temperatures had smaller displacements to failure and hence took somewhat less time.

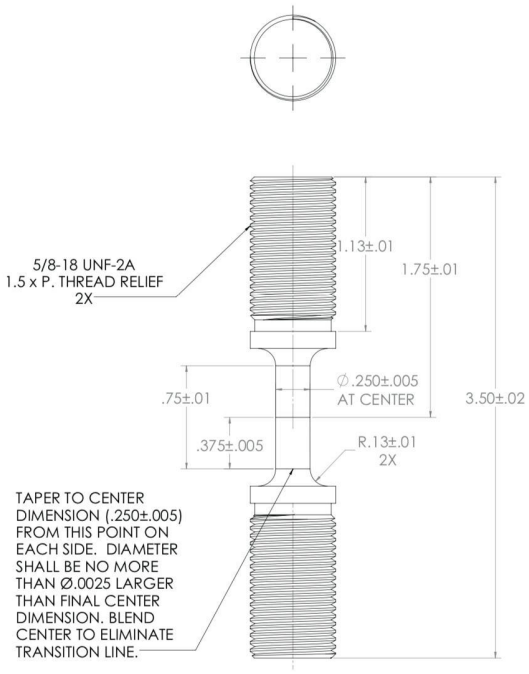

Figure 2-1. Smooth tensile specimen for thermal-mechanical testing of 304L stainless steel.

2.2.2. Sub-Size Uniaxial Tension Specimens for High-Strain-Rate Tests

The rate dependence of 304L stainless steel is another important aspect that needs to be included in the model calibration. Therefore, a series of tests was conducted to explore the rate dependence of this material in a room temperature environment. It is important to remark, however, that the high strain rate response of the material is significantly intertwined with the thermal-mechanical response since rapid plastic deformation increases the temperature in the material. In order to achieve high strain rates in the tests, it is necessary to have specimens with short test gage lengths. A standard specimen that has been used for Kolsky bar testing in the past, shown in Fig. 2-3 [5], was therefore adopted in this study. Figure 2-4(a) shows a schematic of the tensile Kolsky bar test while Fig. 2-4(b) shows a photograph of the specimen mounted in the Kolsky bar. The tensile Kolsky bar is an apparatus that uses the principles of wave propagation to pull the specimen at high strain rates. The set-up used here could apply strain rates between 500 and 3500 1/s.

The specimen is essentially a miniature, or sub-size, tensile specimen of circular cross-section with a nominal test section diameter of 0.125 in. and length of 0.25 in. The diameter of the test section also had a slight taper from the ends to the center. The ends of the specimen had 1/2-20 threads in order to mount the specimen in the test set-ups. In the case of the Kolsky bar, the specimen was threaded into the incident and transmission bars and tightened with half nuts as shown in Fig. 2-4(b). The loading pulse in this set-up is generated by the impact of the striker bar

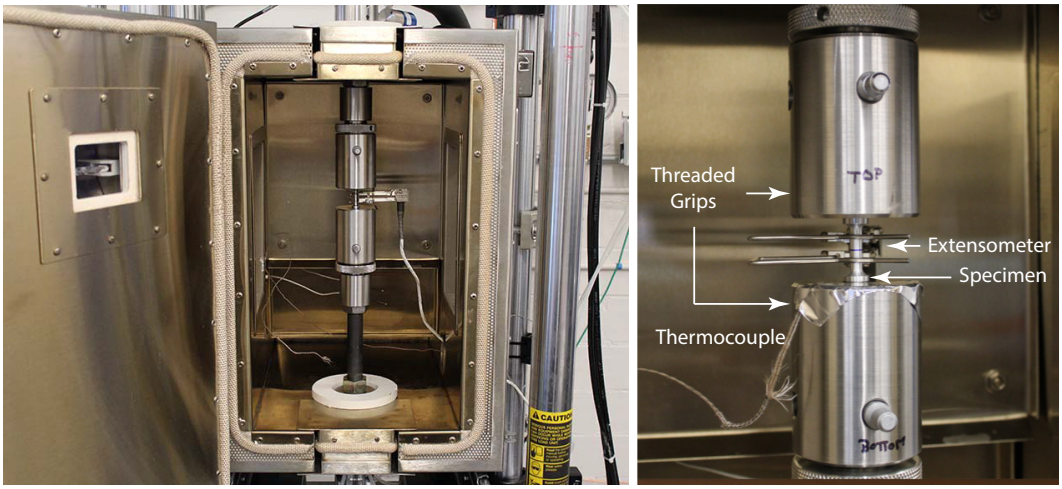

(a) (b)

Figure 2-2. Tensile test set-up with thermal chamber. (a) Overall view of the thermal chamber and (b) test specimen detail.

against the end cap, as shown in Fig. 2-4(a). The pulse propagates down the incident bar and is partially reflected at the location of the specimen. Another part of it is transmitted through the specimen, and a similar interaction occurs at the junction of the specimen with the transmission bar. These interactions had the effect of pulling the specimen to failure in the cases considered here. An optical system measured the stretch in the specimen, while a strain gage measured the strain pulse in the transmission bar. This strain is proportional to the tensile force in the specimen. Reducing the measured data yielded the extension and the force in the specimen as functions of time. The nominal strain rates achieved in the current studies were approximately 1520 and 3440 1/s.

Similar tests were also conducted at slower strain rates using two other set-ups. The first was the 'Dropkinson' bar [6], an apparatus that uses similar principles as the Kolsky bar, but can achieve lower strain rates, from the upper 10s to the mid 100s 1/s. This is accomplished by replacing the incident bar of the Kolsky test with a 'drop-table' machine. The extension in the specimen comes from the same optical measurement system mentioned above, while the load comes from the strain signal in the transmission bar of the apparatus. In this case, testing yielded data at a nominal strain rate of 270 1/s. Finally, using small threaded grips, the specimen was also tested in a uniaxial hydraulic testing machine at strain rates of 0.1 and 3.33×10^{-4} 1/s. In these tests the extension of the specimen was measured using DIC methods and the load using a standard load cell.

2.2.3. Notched Tension Tests for High-Mean-Stress Failure Tests

The principal objective of the tension tests on notched specimens was to generate data to be used in the calibration of the failure model. The design of the notched tension specimens for this project is given in Fig. 2-5. This design allows the specimen to be tested using the same test set-up as in the thermal-mechanical tests, although all tests occurred at room temperature. The

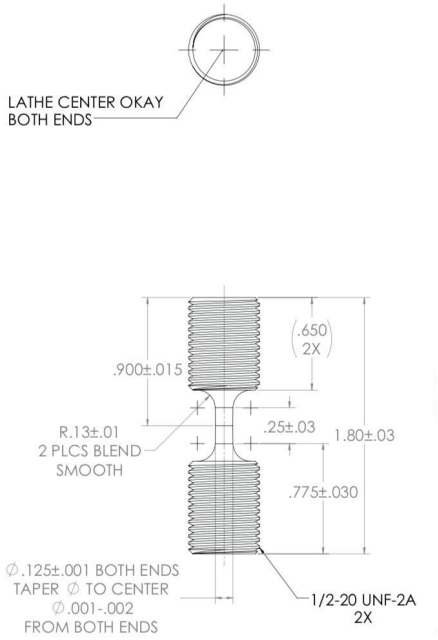

Figure 2-3. Subsize specimen used for high strain rate testing.

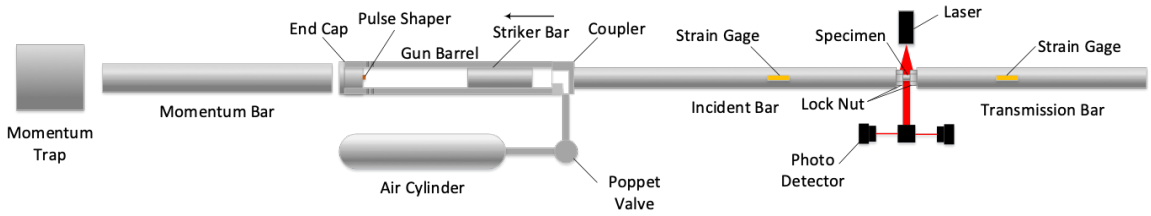

(a)

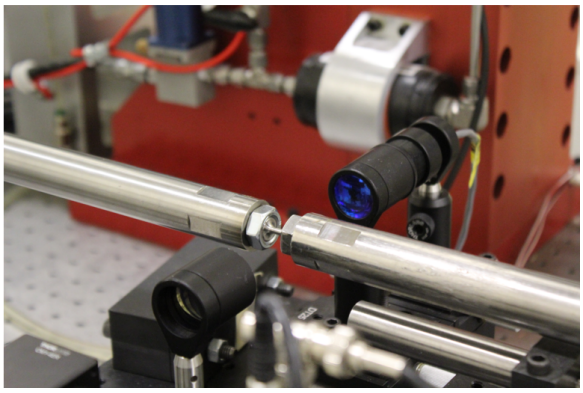

(b)

Figure 2-4. Kolsky bar tests. (a) Schematic of Kolsky bar test and (b) detail of specimen.

commonality between the tests, however, yielded significant time savings. The specimen consists of a test section of circular cross-section with a diameter of 0.394 in. that contains a section of reduced area, or notch, at the center with a minimum diameter of 0.200 in. Specimens with two notch radii, 0.128 and 0.032 in., were tested. Based on the geometry, the plastic deformation is concentrated in the notch while the rest of the test section has little to none. Tensioning the specimen causes the test section and the notch to elongate and contract radially. The material outside the notch, however, contracts less and constrains the contraction of the notch. Therefore, the material in the notch develops tensile stresses in the radial direction that increase the hydrostatic mean stress in the interior. The smaller the notch radius (sharper notch) the higher the constraint, and the higher the hydrostatic mean stress. The mean stress, however, is not constant even in the plane with the smallest diameter. It is highest at the specimen axis and decreases towards the surface. The instrumentation and test control strategy is the same as in the corresponding uniaxial tension tests.

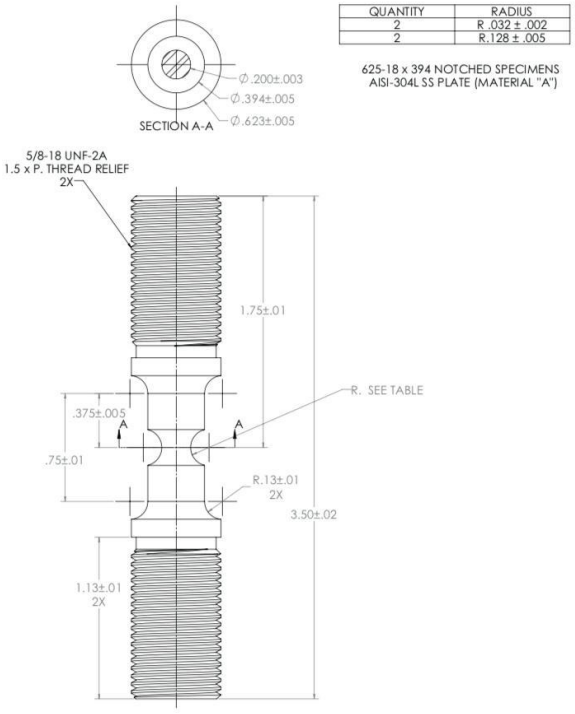

Figure 2-5. Notched 304L stainless steel specimen.

2.2.4. Hat Compression, Shear-Dominated Specimen for Low-Mean-Stress Failure Tests

Whereas the notched tension test specimens are intended to generate values of hydrostatic stress that are higher than in the uniaxial tension test, a more complete calibration of the failure model can be achieved by considering tests in which the hydrostatic stress is below that in the uniaxial tension tests. A specimen design to test the material under shear-dominated loading was originally designed by Brad Boyce and Brad Salzbrenner as the challenge geometry for the 2013

Sandia Fracture Challenge. The behavior of this specimen was studied carefully in [7] and in [8] and afterwards was adopted as a reasonable specimen for model calibration. The specimen design used in this work is shown in Fig. 2-6 while Fig. 2-7 shows the test set-up. The specimen is compressed between two flat platens mounted in a standard testing machine. The instrumentation includes four miniature LVDTs (the second pair is behind the ones shown) that measure the relative displacement of the platens plus a standard load cell to measure the load. The signal from the machine stroke LVDT provides the feedback signal to the test machine controller.

Upon compression, the two narrow sections that join the top, trapezoidal part of the hat to the base are loaded in shear. These will be called the test sections. A particular feature of this specimen that allows it to be used for calibration purposes is that the the radii in the specimen decrease during deformation, thus locally maintaining states of compressive mean stress. This avoids, or at least significantly delays, the development of regions with positive mean stress in the test sections as will be shown later in this report.

A major aspect in the use of the hat specimen is that failure tends to start at the radii of the test sections and in the vicinity of the specimen mid-plane and therefore hidden from direct observation. Furthermore, fracture propagation is initially stable under continued compression. Failure initiation is therefore difficult to detect. The current solution to this issue is to first conduct a test to complete failure, followed by a series of interrupted tests at different levels of compression. The specimens from each interrupted test are then sectioned, polished and imaged with an optical microscope in order to detect the level of compression at which cracks become visible, therefore bracketing the compression levels at which failure initiated. Given time constraints and other practical considerations, however, the number of interrupted tests tends to be limited. Fewer tests lead to larger brackets.

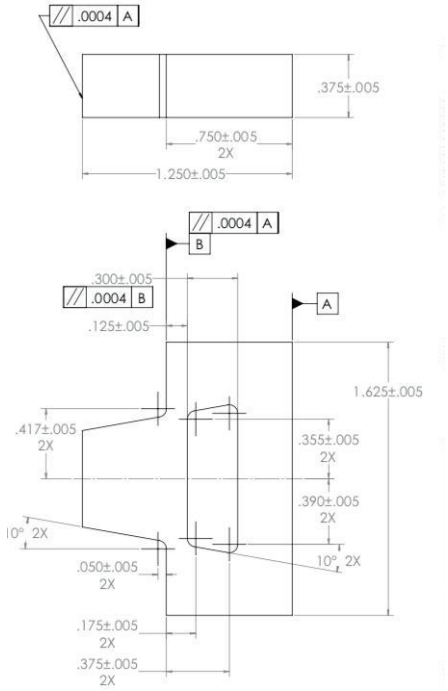

Figure 2-6. Compression top-hat shear specimen.

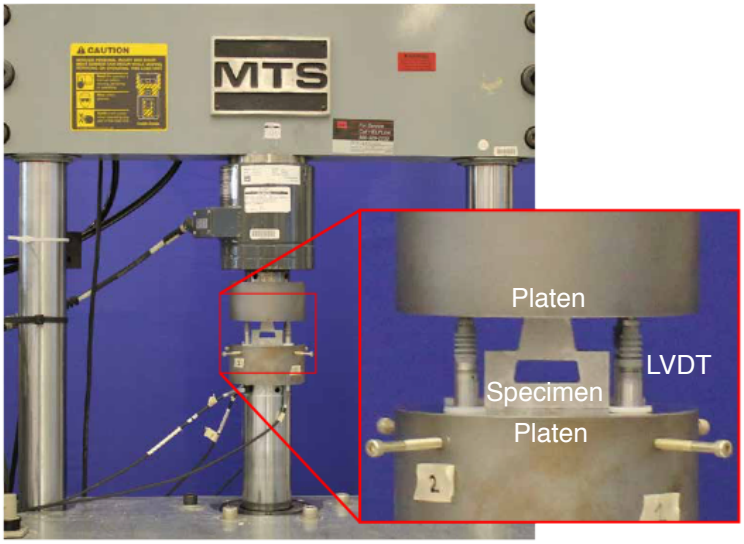

Figure 2-7. Hat specimen compression test.

2.3. Experimental Data

2.3.1. Thermal-Mechanical Tension Test Data

Figure 2-8 presents the engineering stress-strain curves obtained at three temperatures and two nominal strain rates using the standard specimens described previously. Looking first at the slow tests with $\dot{\varepsilon} = 3.33 \times 10^{-4}$ 1/s (solid lines) it is clear that the effect of temperature is to reduce the flow stress of the material as well as the strain to failure as it rises from 30 to 300°C. This is consistent with previous thermal-mechanical testing on 304L by Bonnie Antoun [9]. The jumps in strain towards the end of one of the stress-strain curves at 150°C are likely due to extensometer slippage, but the faint, repeatable, serrations appearing just prior to the ultimate stress in all tests at 300°C may be due to dynamic strain aging, which is known to occur in this material under certain combinations of temperature and strain rate [10]. A final observation is that the scatter between the stress-stain curves at each temperature seems more significant at 300°C.

The tests conducted at a strain rate of 0.1 1/s, in dashed lines, show an increase in the yield stress that seems to become less significant with temperature. This observation was also made in a different test series on 304L sheet in [11]. A second characteristic is that the engineering strain at the ultimate stress and at failure tend to decrease with temperature. This is most obviously seen in the test at 30°C. The latter observation, also seen in [11] is likely due to the temperature increase in the specimen due to heat dissipated by plastic deformation that did not have sufficient time to leave the test section.

2.3.2. Strain Rate Test Data

Figure 2-9(a) shows the engineering stress-strain curves obtained using the sub-scale specimens at 5 values of nominal strain rate spanning 7 decades. The initial temperature in all tests was room

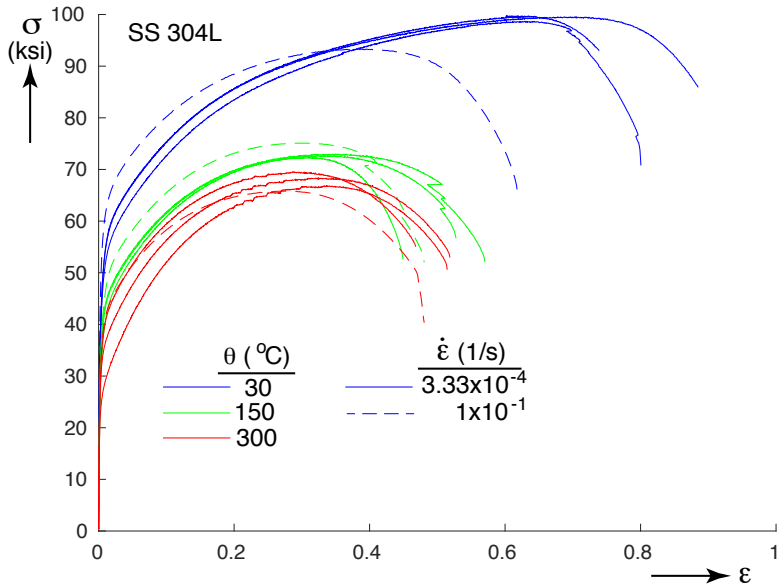

Figure 2-8. Tension test data at several temperatures and strain rates from standard specimens.

temperature. Although the curves do show some scatter, it is relatively minor and they clearly demonstrate a significant rate dependence in the response of the material, showing an increase of about 70% in the yield stress between the extremes. Figure 2-9(b) shows the strain as a function of time for the tests conducted in the Kolsky and Dropkinson bar set-ups. The responses from the Kolsky bar are essentially linear after a transient over the first couple of percent strain, indicating a relatively constant strain rate. The data from the Dropkinson bar show low-frequency oscillations that translate into variations in the strain rate.

2.3.3. Notched Tension Test Data

The load-deflection responses obtained from the tension tests on the notched specimens are shown in Fig. 2-10. These tests were conducted at room temperature. The speed of loading was adjusted depending on the notch so that dividing it by the length of the notch would give a number in the vicinity of the nominal strain rate in the slow uniaxial tension tests, 3.33×10^{-4} 1/s. The values achieved here were 2.5×10^{-4} and 3.2×10^{-4} 1/s for the specimens with notch radius of 0.128 and 0.032 in. respectively . The load in the figure has been divided by the minimum cross-sectional area of the notch A_n. As for many other materials, a sharper notch results in higher loads and smaller displacement to failure. The increase in the load is driven by the high mean stress in the notches.

2.3.4. Hat Compression Test Data

The measured compressive load-deflection response of all hat specimens tested is shown in Fig. 2-11. Note that essentially all curves overlap but that while one displays a maximum in the load

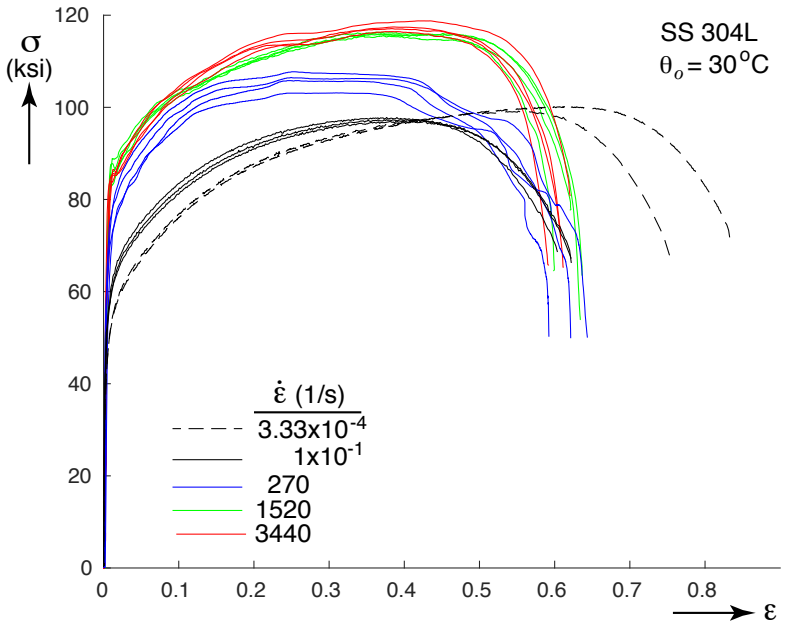

(a)

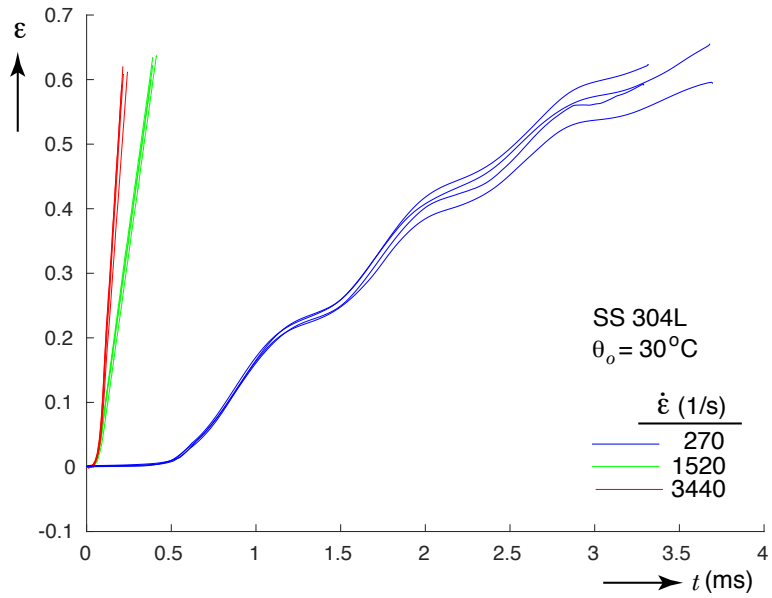

(b)

Figure 2-9. Tension test data at several nominal strain rates from sub-size specimens. (a) Engineering stress-strain response and (b) strain-time history.

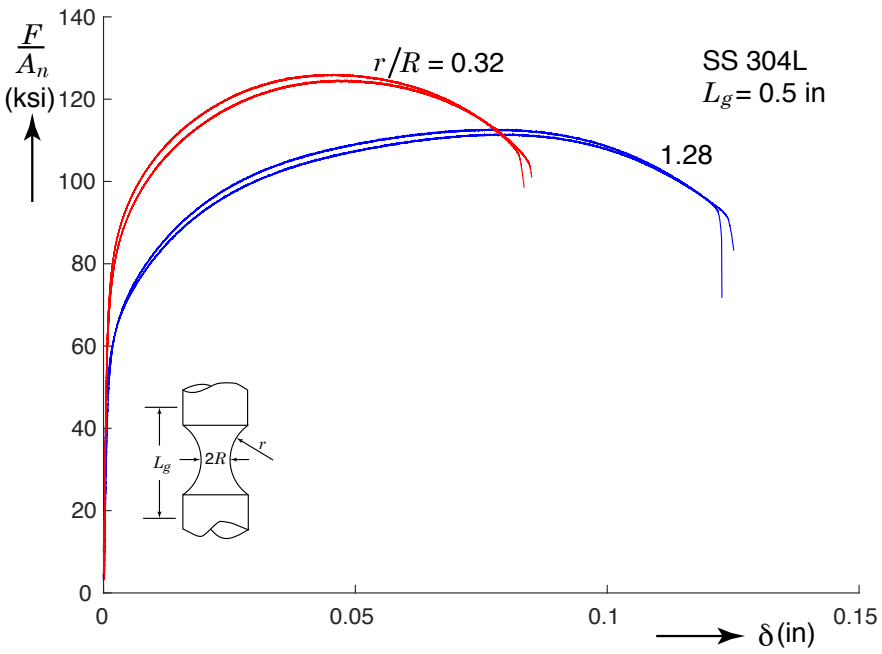

Figure 2-10. Test results for tension tests on notched specimens.

followed by a sharp drop indicating failure of the specimen at $\delta = 0.21$ in., the others are interrupted at different values of displacements. The specimens in these interrupted tests were then sectioned and imaged. The three photos in the figure show a corner of each of the three specimens. The images were taken in a sectioning plane through the mid-thickness of the specimen, where cracks were first detected. The sequence illustrates the development of damage. At $\delta = 0.050$ in. no damage is visible. Small cracks, however, are visible at $\delta = 0.125$ in., which grow significantly by $\delta = 0.175$ in. The conclusion is therefore that material failure likely started at some point between the first two interrupted tests. Given the small crack sizes at $\delta = 0.125$ in., first failure could be taken to have occurred at values just slightly lower.

To illustrate that failure starts at the mid-plane of the specimen rather than at the original flat surfaces, Fig. 2-12 shows photographs of all corners in the test sections of the specimen at $\delta = 0.175$ in. Note that while the photos taken of the mid-section show significant fractures, those at the original surface of the specimen show barely any signs of failure occurring.

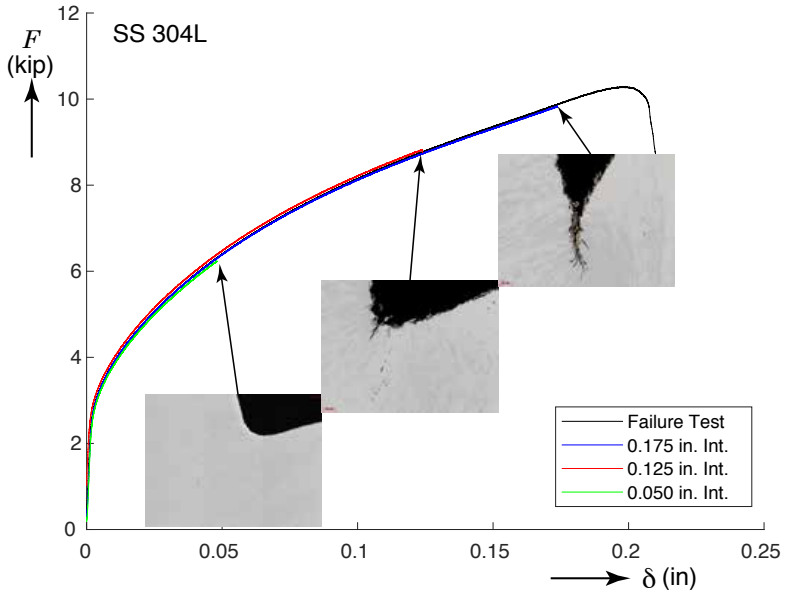

Figure 2-11. Results from tests on hat specimens.

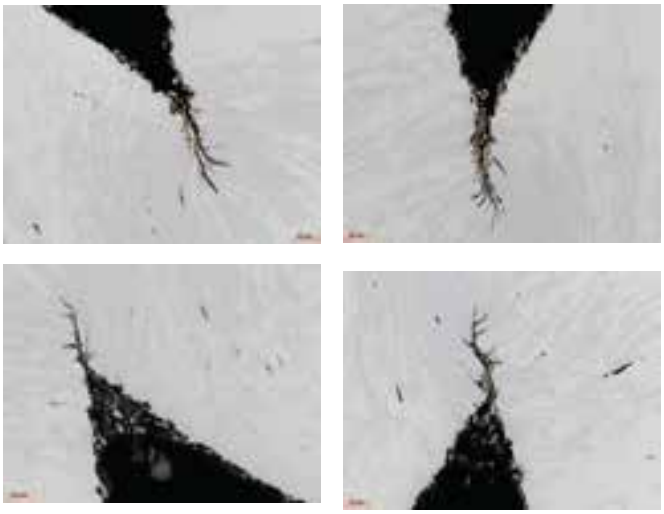

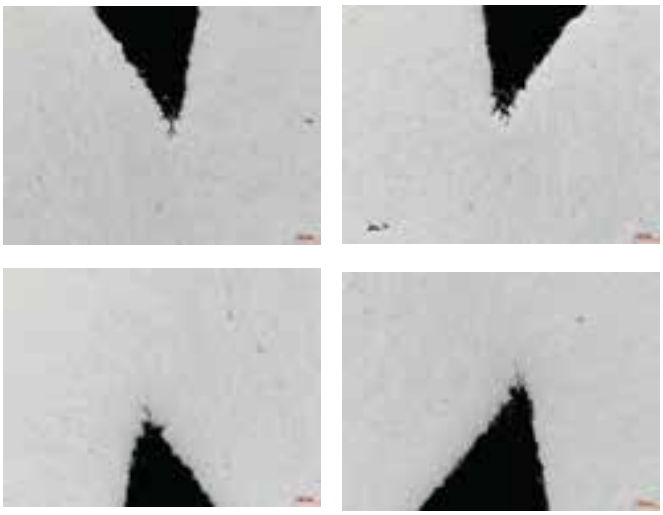

Figure 2-12. Photographs of the four corners in the test sections of the test interrupted at a displacement of 0.0175 in.

3. MATERIAL MODEL CALIBRATION

This section describes the calibration processes for both the elastic-plastic material and failure models. Both account for rate and temperature effects. The theoretical forms of these models are presented in Section 3.1. The subsequent sections discuss calibration procedures with Section 3.4 delving into the approach for the plasticity model and Section 3.5 considers the failure model.

3.1. Thermal-Mechanical Material Model

The elastic-plastic constitutive model calibrated in this work was motivated by previous observations on how the shape of the uniaxial engineering stress-strain curves of 304L stainless steel change with temperature [9], which could not be reproduced sufficiently well by the Johnson-Cook model [12]. The observations motivated a reconsideration of the flow stress form. Specifically, in the original Johnson-Cook form, temperature dependence is included in a purely multiplicative fashion common to all terms. In this way, the same temperature multiplier acts equally on yield, hardening, and rate-dependence. To present a more flexible approach, separate temperature dependencies were considered for each of the terms in the revised flow stress formalism in which a power-law hardening function was used with a Johnson-Cook rate multiplier. This new form was compared to data and explored in Corona *et al.* [11]. Based on these efforts a new *flow-stress parameter* hardening model was added into LAMÉ as a part of the modular plasticity approaches. However, this new form represents a first foray into more flexible temperature-dependent capabilities for these models and as such it has not been documented in the LAMÉ manual [14]. Nonetheless, it is tested under both uniaxial stress and pure shear loadings with different assumed temperature dependencies and at different temperature and rate conditions as described in other documents (*e.g.* [14, 15]). These tests are performed daily through automated Sierra regression test capabilities. As the model has been implemented into the modular plasticity framework, other capabilities such as adiabatic heating [16] and modular failure [17] (which will be discussed later) can be activated. Importantly, this provides substantial flexibility in adapting the specific functionalities and observations to fit the data.

3.1.1. Yield Function and Hardening Rule

A decision was made early in the planning process to assume an isotropic model for the yield (effective stress) function. In LAMÉ, there are two main choices for isotropic yield functions: von Mises and Hosford. The first is quadratic, while the second is non-quadratic and both assume tension-compression symmetry. While advantages have been noted in the choice of non-quadratic and/or tension-compression asymmetric yield functions in other materials, similar observations

are not typically observed in stainless steels. As such, the choice was made to choose von Mises because of its simplicity and applicability. Furthermore, it requires one fewer test for calibration than the other options. As no significant reverse loading is expected in the intended environments, kinematic hardening is neglected and purely isotropic forms are considered.

3.1.2. Hardening Function

The hardening function implemented in this work is based on an approach similar to that of Johnson and Cook [12] in the sense that the hardening modulus depends on three variables: the equivalent plastic strain, $\bar{\varepsilon}^p$, the temperature, θ, and the equivalent plastic strain rate, $\dot{\bar{\varepsilon}}^p$. The Johnson-Cook model uses a multiplicative dependence on these three terms yielding a flow-stress of the form,

$$\bar{\sigma} = \left[\sigma_y + A\left(\bar{\varepsilon}^p\right)^n\right]\left[1 + C\ln\left(\frac{\dot{\bar{\varepsilon}}^p}{\dot{\varepsilon}_o}\right)\right]\left[1 - \theta^{*m}\right], \tag{3.1}$$

where $\dot{\varepsilon}_o$ is a reference strain rate, θ^* is a homologous temperature[1], σ_y is the initial yield stress, and A, n, C and m are fit parameters. The aforementioned flow-stress parameter model modifies this expression by neglecting the explicit temperature multiplier and instead assuming the remaining parameters are each temperature dependent with their own (unspecified) functional forms such that,

$$\bar{\sigma} = \left[\sigma_y(\theta) + A(\theta)\left(\bar{\varepsilon}^p\right)^{n(\theta)}\right]\left[1 + C(\theta)\ln\left(\frac{\dot{\bar{\varepsilon}}^p}{\dot{\varepsilon}_o}\right)\right]. \tag{3.2}$$

As implemented, each of these four functions ($\sigma_y(\theta)$, $A(\theta)$, $n(\theta)$, and $C(\theta)$) are represented as a constant value multiplied by a temperature dependent scaling function. Each of these functions is specified via a Sierra-scope definition and any function that may be defined in that fashion is admissible. This expression allows more flexibility to fit the variation in shape of the uniaxial stress-strain curves observed in testing, provided that suitable forms can be found for temperature dependence.

3.1.3. Adiabatic Heating

A significant part of the work done during plastic deformation of metals is converted to heat. When the deformation is sufficiently slow the heat is dissipated to the surroundings at a sufficiently fast rate to keep increases in temperature small. At higher loading rates, however, the temperature will increase, and at Kolsky bar rates the process can be considered adiabatic. In a truly thermal-mechanical analysis, a heat transfer analysis needs to be coupled with the mechanical model to determine the temperature of the material. Without a heat transfer analysis,

[1] $\theta^* = (\theta - \theta_{\text{ref}})/(\theta_{\text{melt}} - \theta_{\text{ref}})$ where θ_{ref} is a reference temperature and θ_{melt} is the melting temperature.

the analysis becomes restricted to two extremes: isothermal or adiabatic. The conversion of plastic work to temperature rise in the material can be written as [16]:

$$\theta = \theta_o + \frac{\beta^{TQ}}{\rho c_p} \int_{t_o}^{t} \dot{W}^p \, dt \tag{3.3}$$

where ρ is the density of the material, c_p is the specific heat capacity, $\dot{W}^p$ is the rate of plastic work per unit volume and β^{TQ} is the Taylor-Quinney coefficient, a parameter that determines the fraction of plastic work converted to heat. Both the initial density of the material and the specific heat capacity are usually taken from handbook values, but the value of the Taylor-Quinney coefficient has to be measured experimentally as in [18]. Such measurements, however, are difficult and the value is generally assumed or calibrated indirectly as will be done here.

3.2. Ductile Failure Model

Ductile failure usually refers to fracture after significant plastic deformation. In general, ductile failure has the objective of modeling the initiation of failure as well as its propagation, usually in finite element models. Unlike fracture mechanics methods, ductile failure methods do not require the presence of a flaw in the structure. Instead they utilize a damage parameter that accumulates with plastic deformation. Initiation of failure is declared when the damage parameter reaches a critical value. The propagation of fracture requires a method to modify the finite element mesh, with element deletion being the simplest and probably most widely used one. Since fracture is a highly localized process, clearly the results will be highly dependent on the element size and associated energetic considerations. The model calibrated here is intended solely to address fracture initiation.

Ductile failure models are mostly based on experimental observations and to a lesser degree on results from theoretical calculations. The models used at the structural level are therefore empirical in nature but have forms that accommodate both experimental and theoretical inputs. Briefly, ductile failure can be strongly dependent on the history of the mean (or hydrostatic) stress during loading. Generally, the higher the mean stress, the faster the damage accumulates. While some models use the mean stress directly, others use the triaxiality, defined as the ratio of the mean stress to the von Mises stress. The history of the Lode angle, which is the angle in the π-plane between the projections of the principal stress vector and the major principal stress axis, is another parameter that is thought to influence failure. Generally, the closer the projection of the state of stress is to pure shear, the faster the damage accumulates. Alternatively one can think of failure as being dependent on the history of the first invariant of the stress tensor, I_1 and of two invariants of the deviatoric stress tensor, J_2 and J_3.

In addition to the stress history, the damage accumulation in the material may also be a function of the strain rate and of the temperature histories during loading. Hence, a modular approach to failure is also desirable in order to choose the functional dependency of the damage accumulation on the stress, equivalent plastic strain rate, and temperature histories. In this approach the damage D is calculated as

$$D = \frac{1}{d_{crit}} \int_0^{\bar{\varepsilon}^p} w_1(p)\, w_2(\theta_L)\, w_3(\eta)\, w_4(\dot{\hat{\varepsilon}}^p)\, w_5(\theta)\, d\hat{\bar{\varepsilon}}^p, \tag{3.4}$$

where d_{crit} is the critical damage value, p is the mean stress, θ_L is the Lode angle, and η is the triaxiality. The modular approach allows the user to choose which combination of these five functions to include in the expression as well as different choices for the functional form of each. For a complete description, see [17].

3.3. Fixed Parameters

The J_2 plasticity model contains a set of parameters that are independent of plastic deformation and are taken as pre-defined constants during the calibration process. These include the density, ρ, the two elastic constants Young's modulus and Poisson's ratio, E and ν, and the specific heat capacity c_p. The values of these parameters are given in Table 3-1.

Table 3-1. Material parameters independent of plastic deformation in lb-in-s system of units. 1 lb = 1 blob$\times$1 in/s^2.

Parameter	ρ, blob/in^3	E, psi	ν	c_p, in-lb/(blob °C)
Value	7.49×10^{-4}	28×10^6	0.27	0.776×10^6

3.4. Hardening Function Calibration

The first step in the calibration of the hardening function in (3.2) is to find values for the power-law hardening parameters $\{\sigma_y, A, n\}$ from the stress-strain curves obtained at each temperature. In other words, the fits are carried out for each temperature independently of the others. To do this, the curves with $\dot{\varepsilon} = 3.33 \times 10^{-4}$ 1/s and with the highest strain to failure in Fig. 2-8 were selected as the target curves for the calibration. Because of the low strain rate and the long duration of the tests, the temperature rise in the specimen due to plastic deformation is likely very small due to heat loss in the specimen through conduction, convection and radiation [18]. Therefore, an isothermal assumption was made during calibration.

While values for optimal parameters can be found rather easily for data up to the ultimate stress, conducting a calibration that covers the post-ultimate-stress requires a trial-and-error approach together with a finite element model of the test specimen. The geometry and mesh of the model used in the thermal-mechanical tests is shown in Fig. 3-1(a). It is intended to replicate the dimensions of the test-section of the specimen in Fig. 2-1, taking advantage of three planes of symmetry. It is slightly tapered from the top to the bottom, where the plane of symmetry that splits the length in two is located. A node set located 0.25 in. above this plane represents the location of one of the edges of the extensometer. The nominal element size is 0.01 in. on the side.

The procedure consisted of trying different combinations of $\{\sigma_y, A, n\}$ until reasonable fits were obtained at each temperature. The final selected values are in the columns to the left in Table 3-2, while fig. 3-1(b) shows the comparison between tests and the calibrated simulations. In general the fits are reasonable. Because of the form of the power-law-hardening, in order to capture the drop in engineering stress after ultimate, the calculated curves are above the measured ones for strains below approximately 0.25.

In order to interpolate the values of the power-law-hardening parameters in the power-law-parameter model, first they are defined as

$$\begin{aligned} \sigma_y(\theta) &= \sigma_y(30) m_{\sigma_o}(\theta) \\ A(\theta) &= A(30) m_A(\theta) \\ n(\theta) &= n(30) m_n(\theta). \end{aligned} \tag{3.5}$$

(3.6)

where m_{σ_y}, m_A and m_n are piecewise linear functions of θ with the segment endpoints given in the right columns in Table 3-2. The melting point temperature 1400°C is included as the highest temperature to bring the strength of the material to zero. This is done in case the temperatures during an analysis go slightly above 300°C but, without data to support it, this is just an approximation. At the opposite end, this model calibration must not be used for temperatures lower than room temperature.

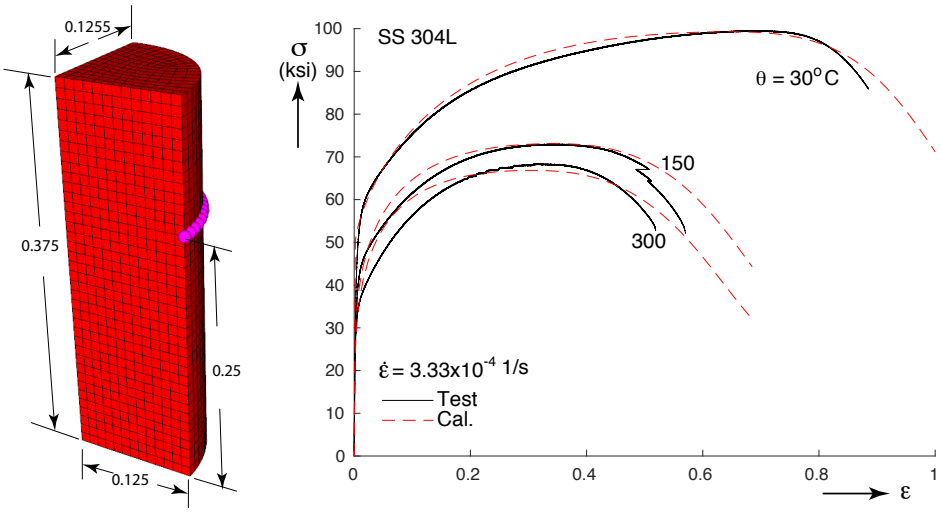

Figure 3-1. Uniaxial tension tests. (a) Finite element model for the thermal-mechanical tests and (b) comparison of power-law hardening calibrated predictions at 30, 150 and 300°C to test data.

Once the thermal calibration of the model has been established, the next step is to consider the behavior of the material at fast strain rates. This includes the calibration of two parameters. The first is the strain rate function $C(\theta)$ in (3.2) while the second is the Taylor-Quinney coefficient in (3.3).

Table 3-2. Power law hardening parameter values at three temperatures.

T_o, °C	σ_y, ksi	A, ksi	n	m_{σ_y}	m_A	m_n
30	50	188	0.72	1	1	1
150	20	123	0.37	20/50	123/188	0.37/0.72
300	10	115	0.30	10/50	115/188	0.30/0.72
1400	-	-	-	0	0	0

Looking first at the calibration for C the reference strain rate was taken as the slowest strain rate in the tests, so $\dot{\varepsilon}_o = 3.33 \times 10^{-4}$. After that, an initial guess for a constant C was taken by measuring how the stress at a strain of 0.1 increased with strain rate in Fig. 2-9(a). This gave a value of $C = 0.022$. At the same time, the data in Fig. 2-8 and previous observations from [11] suggest a decreasing trend in C with temperature. Based on these

$$C(\theta) = C(30) * m_C, \tag{3.7}$$

where the multiplier m_C was taken as in Table 3-3. This initial guess, however, needs to be updated by taking into account both the response of the specimens over the complete strain ranges in the stress-strain curves and the interaction between the rate effects and the temperature rise. To achieve this, finite element simulations of the high strain rate tests is necessary. The geometric model of the specimen is shown in Fig. 3-2(a). The elements in the test section are hexahedral with 10 elements along the length and four through the radius (0.025 in. by 0.015 in.). A second model with elements half of this size showed that reasonably well converged results were produced by the coarser mesh.

Table 3-3. The multiplier function m_C.

θ °C	30	150	300	1400
m_C	1	0.5	0.1	0.

The calibration of the Taylor-Quinney coefficient was also achieved indirectly in these simulations. The initial guess for the coefficient from [11] was 0.6. The comparisons between the predictions of the calibrated model and the test data at 1500 1/s, however, were improved by choosing $\beta_{TQ} = 0.5$ instead. Dropping the value of $C(30)$ to 0.016 also improved the comparisons of the simulations to the tests. The predictions for all cases are shown in Fig. 3-2(b). All but the case with $\dot{\varepsilon} = 3.33 \times 10^{-4}$ were run as adiabatic calculations. The temperature in the models rose from 30 to approximately 200°C, well within the range of the thermal-mechanical calibration range. The results show that, in general, the calibrated model can follow the test results relatively closely over the complete strain range. At this point, all the parameters of the hardening rule, including the temperature functions have been determined.

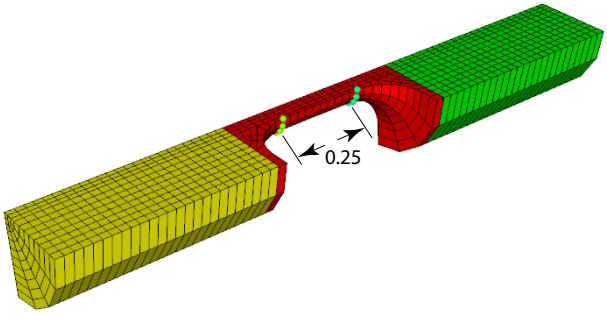

(a)

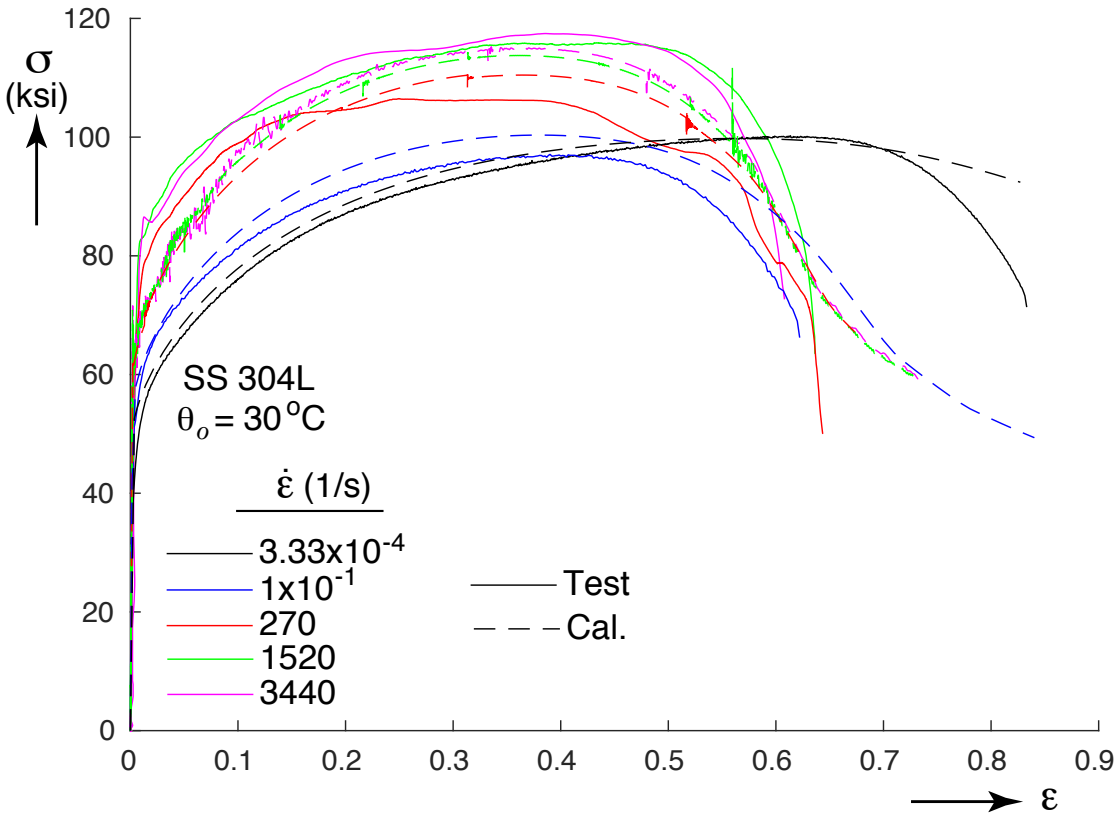

(b)

Figure 3-2. Uniaxial tension test simulations for strain rate dependence calibration. (a) Mesh of sub-size specimen with yellow and green blocks as rigid bodies and (b) comparison of calibrated predictions at five strain rates to test data.

3.5. Failure Model Calibration

Once the hardening function parameters have been determined, the next step is to choose and calibrate a failure model. Previous experience modeling the failure of 304L stainless steel indicated that using a constant value of equivalent plastic strain at failure may be a good choice for this alloy [19]. Therefore, the attempt was made to see if such failure criterion may fit the test data. In addition the effect of temperature and strain rate on ductile failure also need to be addressed, as will be demonstrated later in this section.

Concentrating first on failure at very low rates of loading, where isothermal models are more appropriate, the set of specimens used included two notch test geometries, one hat compression geometry and the uniaxial tensile geometry. The first step in the calibration process consists of making finite element models of the specimens used in the laboratory that are meshed finely enough to provide reasonably converged results. The element sizes were based on previous simulations. All calculations are conducted using selective deviatoric elements. The element damage outputs reported correspond to the average of the damage calculated at the eight integration points.

The first tests considered are the tension tests on notched specimens. Figure 3-3(a) and (b) shows the finite element models. Note that the models take advantage of three planes of symmetry, so only 1/8 of the specimen needs to be modeled. The rows of spheres represent node sets used to extract displacements that could be compared to the extensometer measurements during the tests. The element size in these models is such that 16 elements fit along the minimum radius of the specimen.

Figure 3-3(c) shows the predictions of the load-deflection response in dashed lines together with the experimental results in solid line. Clearly, the predicted loads are higher than the measured ones. This is likely the result of using the relatively simple J_2 plasticity model. This point is a fork in the calibration process. One path is to keep the calibration of the hardening function as-is and accept the differences in Fig. 3-3. The second one is to modify the hardening function calibration to generate better results for these tests even if we have to accept more difference between test and analysis results in Fig. 3-2. For the latter option, Fig. 3-3(d) shows new predictions obtained by dropping the parameter σ_y from 50 ksi to 42.5 ksi.

Considering the compression hat specimen next, Figs.3-4(a) and (b) show the mesh used in the model globally and in the vicinity of the test section. This model takes advantage of the two planes of symmetry in the specimen. The nominal element size in the test section is 0.002 in. and the mesh becomes progressively coarser away from the test section. Figures 3-4(c) and (d) show comparisons of the calculated load-deflection responses obtained using the as-calibrated hardening function and using the reduced σ_y of 42.5 ksi. Again, the original fit overestimates the force significantly more than the case with $\sigma_y = 42.5$ ksi.

In the current work, the choice of $\sigma_y = 42.5$ is adopted to continue the calibration. The effect of this change in the predicted stress-strain curves first shown in Fig. 3-2 is shown in Fig. 3-5. Note that all predicted stress-strain curves now lay below the measured ones. At the same time, the strain at ultimate increases somewhat as well. Although the latter effect could be corrected by further iteration, the changes are moderate enough to still accept the results.

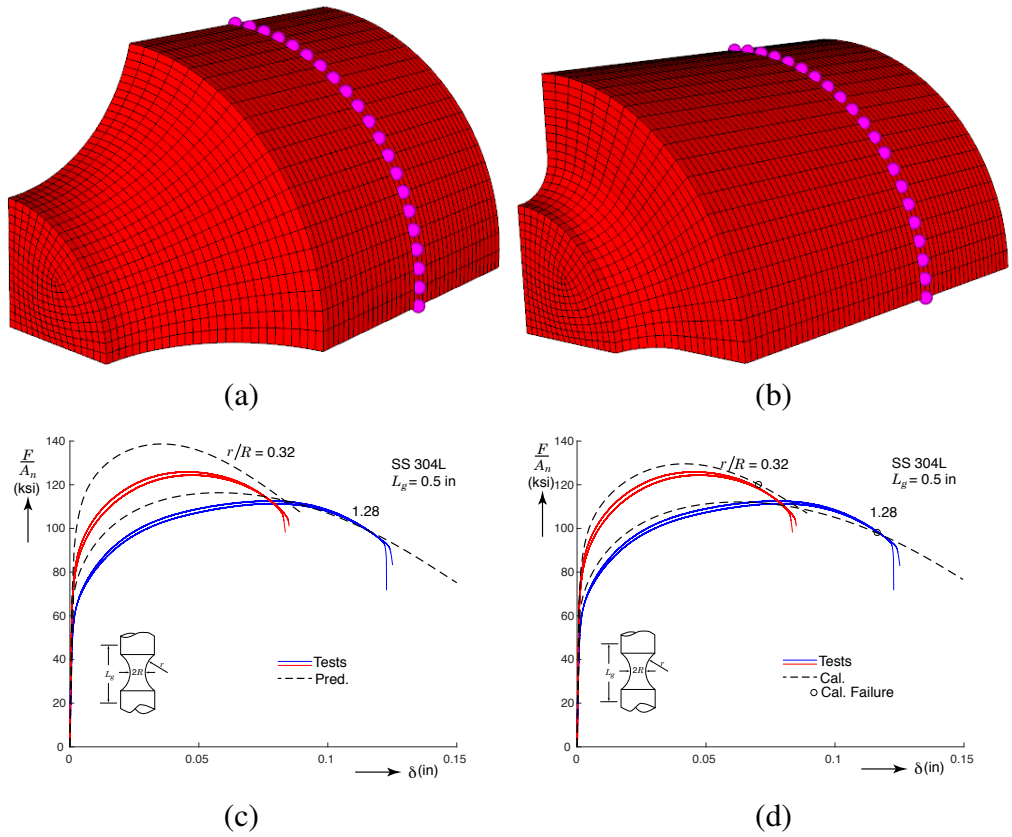

Figure 3-3. Notched tension specimens. (a) Mesh for specimens with $r/R = 1.28$, (b) mesh for specimens with $r/R = 0.32$, (c) prediction vs. test comparison with the original fit (d) prediction vs. test comparison with the modified fit.

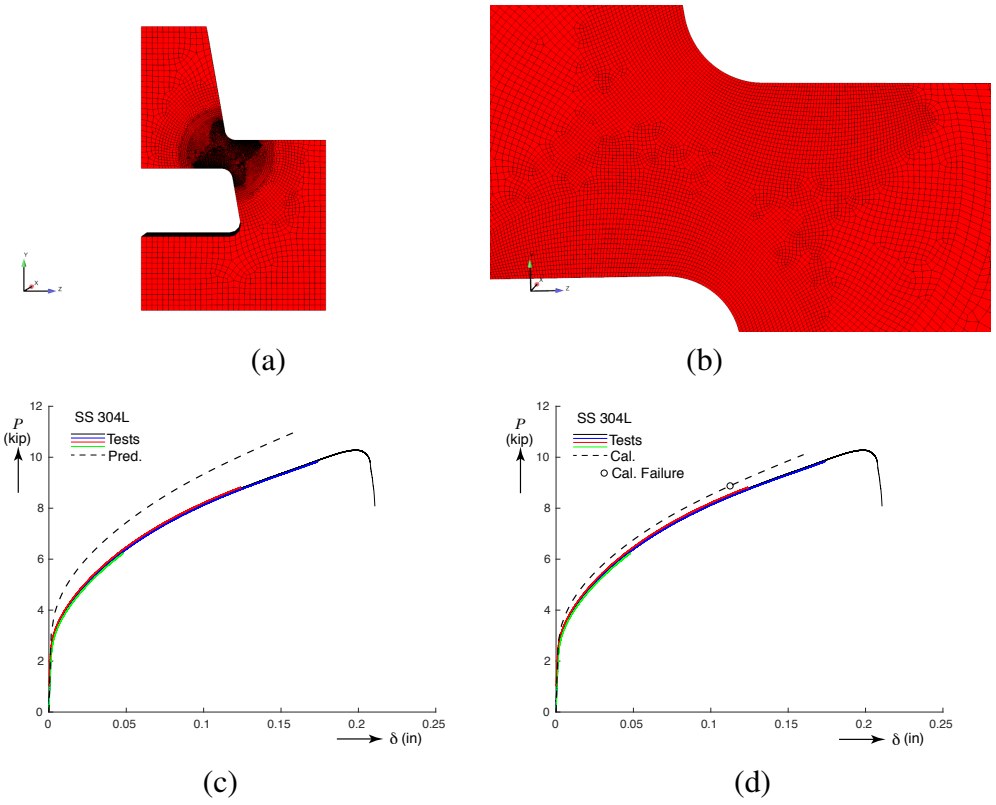

Figure 3-4. Hat compression tests. (a) Model mesh, (b) detail in the test section, (c) prediction vs. test comparison with the original fit and (d) prediction vs. test comparison with modified fit.

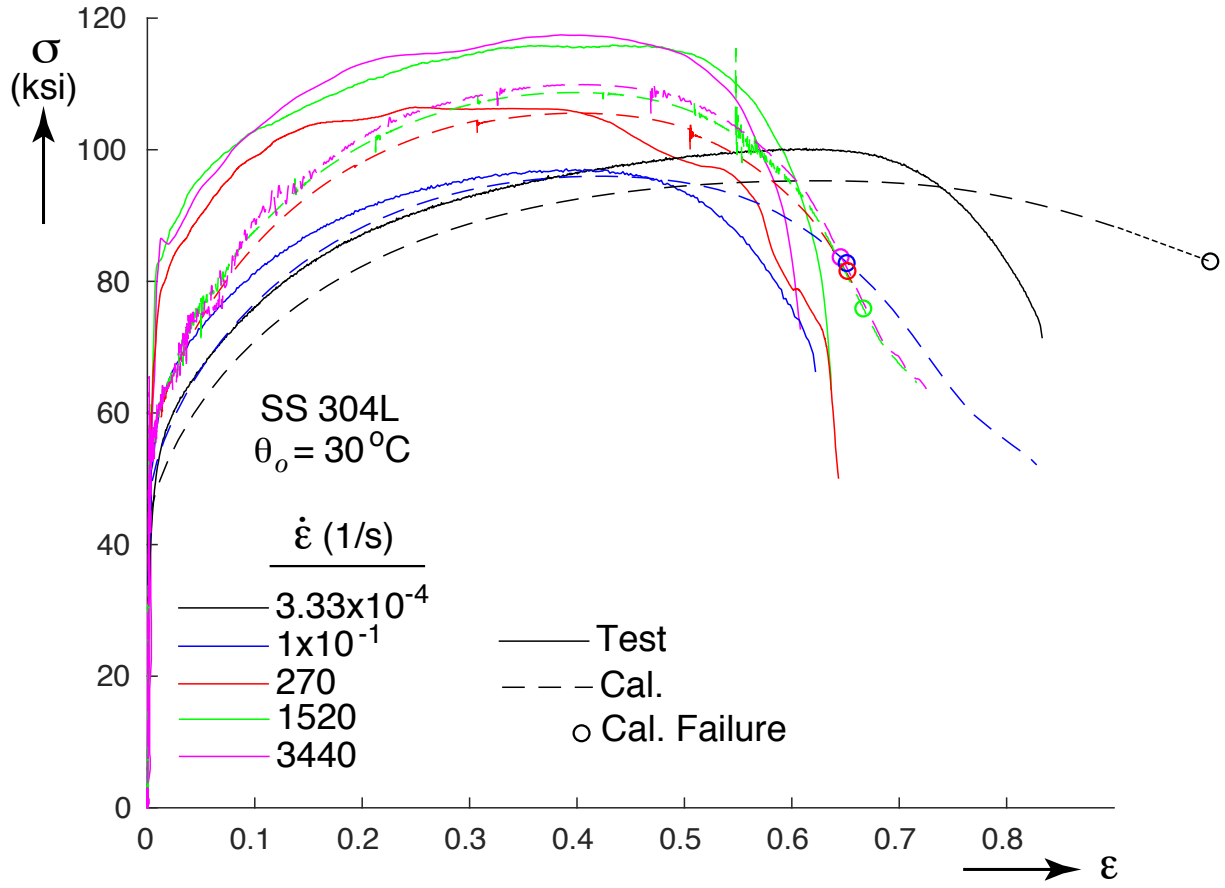

Figure 3-5. Comparison of calibration stress-strain predictions to test data for five strain rates.

From the initial calibration of the uniaxial tension test with $\dot{\varepsilon} = 3.33 \times 10^{-4}$ and $\theta = 30°\text{C}$ a critical value of equivalent plastic strain of 1.13 seemed reasonable and was kept as the first value to be tried when determining the rate and temperature dependence of failure. Under these conditions, the failure model in (3.4) to be investigated can be written as

$$D = \frac{1}{d_{crit}} \int_0^{\bar{\varepsilon}^p} w_4(\dot{\bar{\varepsilon}}^p)\, w_5(\theta)\, d\hat{\bar{\varepsilon}}^p \tag{3.8}$$

where $d_{crit} = 1.13$ and w_4 and w_5 are given as tabular functions in Tables 3-4 and 3-5 to generate the appropriate changes in the engineering strains to failure in the various uniaxial tension tests conducted. The tabular function for w_5 needs to be generated first based on the uniaxial tension tests conducted at the reference strain rate of $\dot{\varepsilon} = 3.33 \times 10^{-4}$ so that the initiation of failure occurs at the points marked with solid circles in Fig. 3-6 . The point at 30°C is of course fixed by the value of d_{crit} and w_5 reduces the strain to failure at higher temperatures.

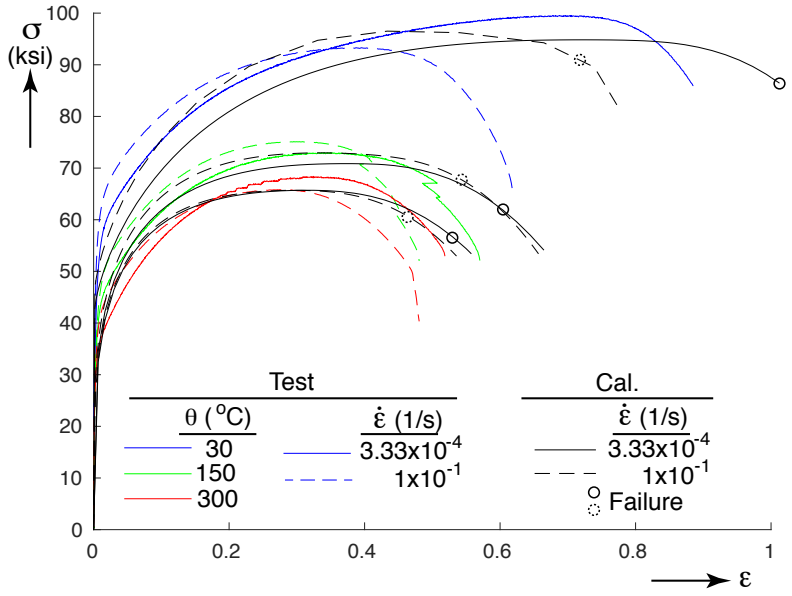

Figure 3-6. Comparison of calibration stress-strain predictions to test data for three temperatures and two strain rates.

Table 3-4. Values for the function $w_5(\theta)$.

$\theta\,°\text{C}$	30	150	300
m_θ	1	1.27	1.34

Table 3-5. Values for the function $w_4(\dot{\bar{\varepsilon}}^p)$

$\dot{\bar{\varepsilon}}^p$	3.33×10^{-4}	0.1	217	1500	3500
$m_{\dot{\bar{\varepsilon}}^p}$	1.0	1.4	1.25	1.25	1.25

Once w_5 has been calibrated, the values of w_4 are determined from the experimental stress-strain curves at the faster strain rates so that the decrease in strain to failure occurs as given by the circles in Fig. 3-5, which were all close to each other as shown in the figure.

The next step is to go back to the notched and hat specimens to verify the assumption that failure at a constant value of equivalent plastic strain provides a good fit to the displacements at which failure occurred in the tests. Figure 3-3(d) shows with circle symbols the points in the load-deflection curves at which failure was detected in the notched specimens. Here, failure was detected at slightly smaller displacements than in the experiments, 94% and 83% of the measured values for $r/R = 1.28$ and 0.32, respectively. Figure 3-7 shows the damage accumulation painted on the deformed specimen shapes at the step when the damage first exceeded a value of 1. In both cases the rim of the smallest cross-section reached $D = 1$ before the rest of the specimen. This is in contrast to the uniaxial tension tests where $D = 1$ occurs first at the center of the specimen.

For the hat compression test, Figure 3-4(d) shows the point in the load-deflection response at which the damage reached one, at a displacement of 0.112 in. Recall that the conclusion from the test data was that failure initiated at a displacement smaller, but near 0.125 in. Figure 3-8 shows that $D = 1$ was first exceeded at the same location where damage was first visible in the experiments. Finally, Fig. 3-9 presents plots of the evolution of the equivalent plastic strain as functions of triaxiality for the uniaxial tension test, the two notched tension specimens and the hat compression test at the element where D first reached a value of one. The circles show the points where $D = 1$ while the crosses show the points where the displacement in the simulations reached the values where the test specimens first exhibited failure. As expected, all the circles occur at $\bar{\varepsilon}^p = 1.13$ at points relatively close to the crosses. Note that while the point of failure is slightly underestimated for the hat and notched specimens, it is overestimated by about the same margin for the uniaxial specimen. All in all, using a constant value of $\bar{\varepsilon}^p$ seems to give reasonable failure criterion that matches all the available data well.

Finally, the failure data marked in Fig. 3-6 shows that the model does reasonably well when the temperature initial conditions changed from 30 to 150 and 300°C. In all cases the reduction in the strain at failure at the higher loading rate with respect to the lower one is very close to that seen in the experiments. In absolute terms, the strains at failure are somewhat over-predicted in all cases as explained previously.

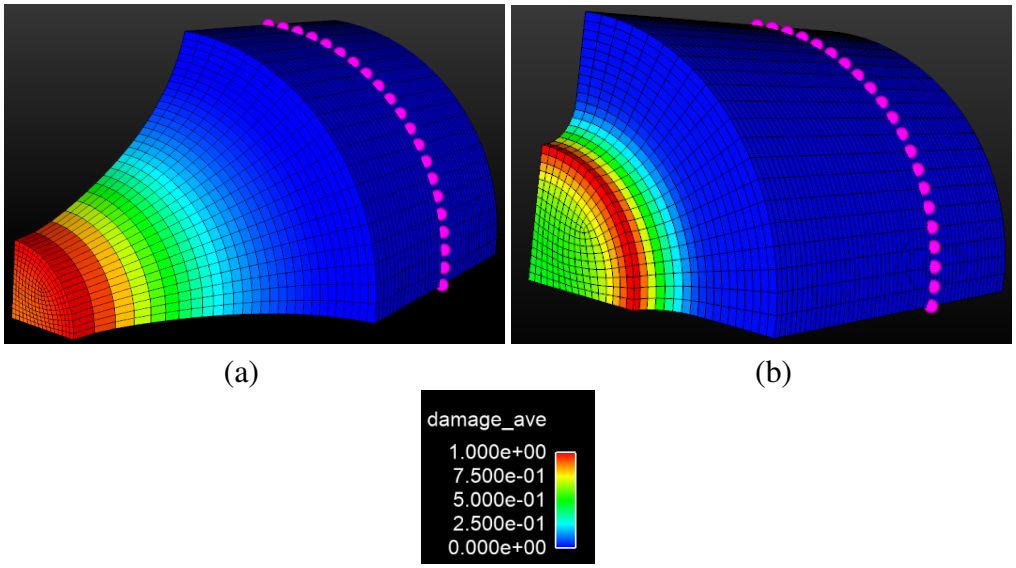

Figure 3-7. Damage levels at predicted failure. (a) $r/R = 1.28$ **and (b)** $r/R = 0.32$**.**

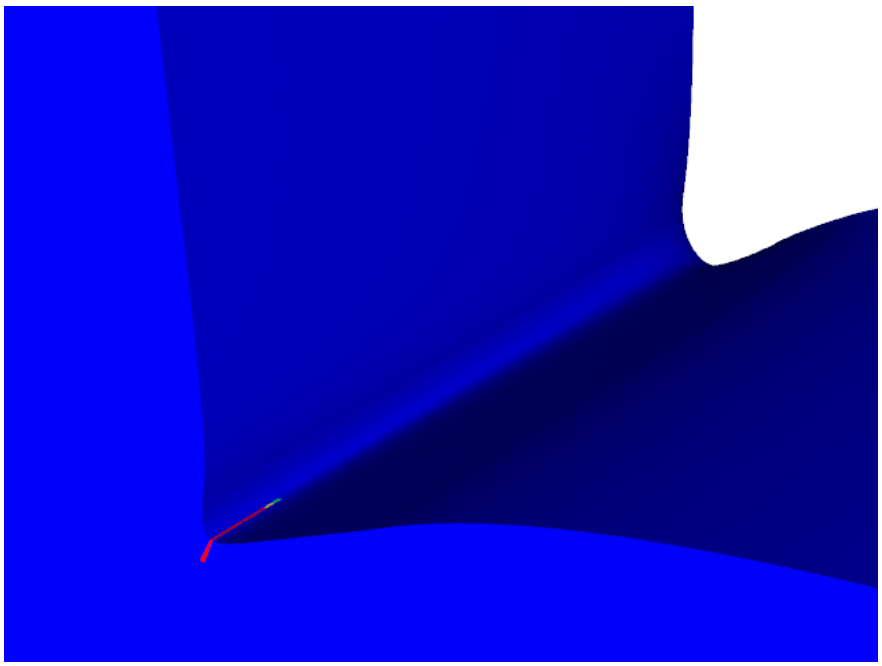

Figure 3-8. Detail showing the region in the hat specimen where the damage first became critical in red at the mid-plane.

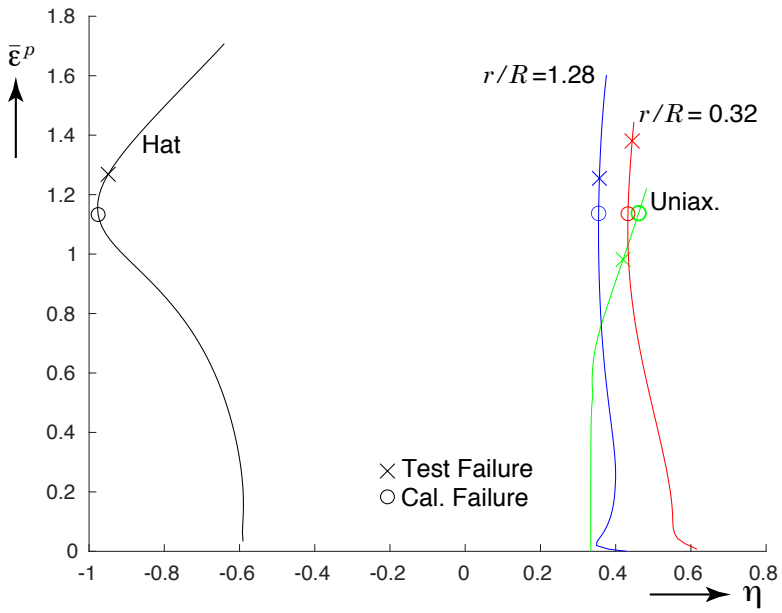

Figure 3-9. Equivalent plastic strain vs. triaxiality histories at the elements that reached a damage on one first.

4. UNCERTAINTY CHARACTERIZATION

The calibrations presented in the previous sections were carried out in a deterministic manner, with single values assigned to each parameter. In reality, variability from experiment to experiment can be seen in just about any of the test data sets presented, which can be due to actual small differences among the material samples and tests and, to a smaller degree, uncertainties associated with the collection of data. Another source of variation appears when materials from different heats and manufacturers, or lots, are considered. An example of variability between plates from two lots was presented in Fig. 1-2, which shows a greater difference between lots than among repeats with specimens from a single plate as in Figs. 2-8 and 2-9(a). Based on these observations, the calibrations presented here cannot be representative of all 304L stainless steel lots. Limits in the possible range of the model parameters, however, can be proposed assuming that the lot-to-lot variability is dominant.

In this section, uncertainty estimates will be developed for parameters in the hardening function (3.2) and for the value of damage at failure (3.8). The first will be based on data gathered from three similar calibrations that have been conducted for different lots of 304L stainless steel. The second, however, is heuristic in nature since the evidence available at this time is limited.

4.1. Hardening Rule

The uncertainty in the hardening rule parameters can be incorporated in the analysis in several ways. The method chosen here is to modify the multiplier functions in (3.5) and (3.7) using "gain" factors as follows:

$$\begin{aligned} \bar{m}_{\sigma_y} &= G_{\sigma_y} m_{\sigma_y} \\ \bar{m}_A &= G_A m_A \\ \bar{m}_n &= G_n m_n \\ \bar{m}_C &= G_C m_C, \end{aligned} \tag{4.1}$$

where the $\bar{m}$s are the modified multiplier functions and the Gs are the gains. The objective is now to determine lower and upper bounds for the gain factors based on a collection of data from different lots.

4.1.1. Lot-to-Lot Variability

Three calibrations are considered for uncertainty estimation: the present one, one conducted on 0.062 in. thick sheet using data from [18] and calibrated in [11], plus another on specimens

extracted from a tube of diameter 3.5 in. and thickness 0.188 in. [20] and calibrated in [9]. Tables 4-1 through 4-3 show the values of each of the hardening function parameters and the Johnson-Cook rate parameter, calibrated at each temperature. The values in the tables are also plotted in Fig. 4-1. Note that while the data show variability, definite trends can still be discerned for each parameter as the temperature changes.

Table 4-1. Hardening function parameters for the current work.

$\theta\,^\circ$C	σ_y, ksi	A, ksi	n	C
30	50	188	0.72	0.016
150	20	123	0.37	0.008
300	10	115	0.30	0.0016
30 (2019)	25	207	0.65	-

Table 4-2. Hardening function multipliers for 304L stainless steel 0.062 in. thick sheet from [11].

$\theta\,^\circ$C	σ_y, ksi	A, ksi	n	C
30	40	189	0.635	0.021
150	20	121	0.345	0.012
300	7.8	113.5	0.237	0.

Table 4-3. Hardening function multipliers for 304L stainless steel tube from [9]. Values interpolated between measurement points at 30, 100, 200 and 400°**C.**

$\theta\,^\circ$C	σ_y, ksi	A, ksi	n	C
30	50	168	0.69	-
150	20	127	0.39	-
300	8	121	0.32	-

4.1.2. Calculation of Gain Bounds

The upper and lower bounds of the gains were calculated based on the data presented in Tables 4-1 through 4-3. Other historical values of σ_y were also considered, one of which had a value of 66.5 ksi, which is higher than those in the tables adopted. The bounds relate directly to the data in the tables and from (3.5) and (4.1) and are given by [21]

$$
\begin{aligned}
G_{\sigma_y}^{\text{lower}} &= \min_i \left[\frac{\min_j \sigma_y^j(\theta_i)}{\bar{\sigma}_y m_{\sigma_y}(\theta_i)} \right] \\
G_{\sigma_y}^{\text{upper}} &= \max_i \left[\frac{\max_j \sigma_y^j(\theta_i)}{\bar{\sigma}_y m_{\sigma_y}(\theta_i)} \right]
\end{aligned}
\tag{4.2}
$$

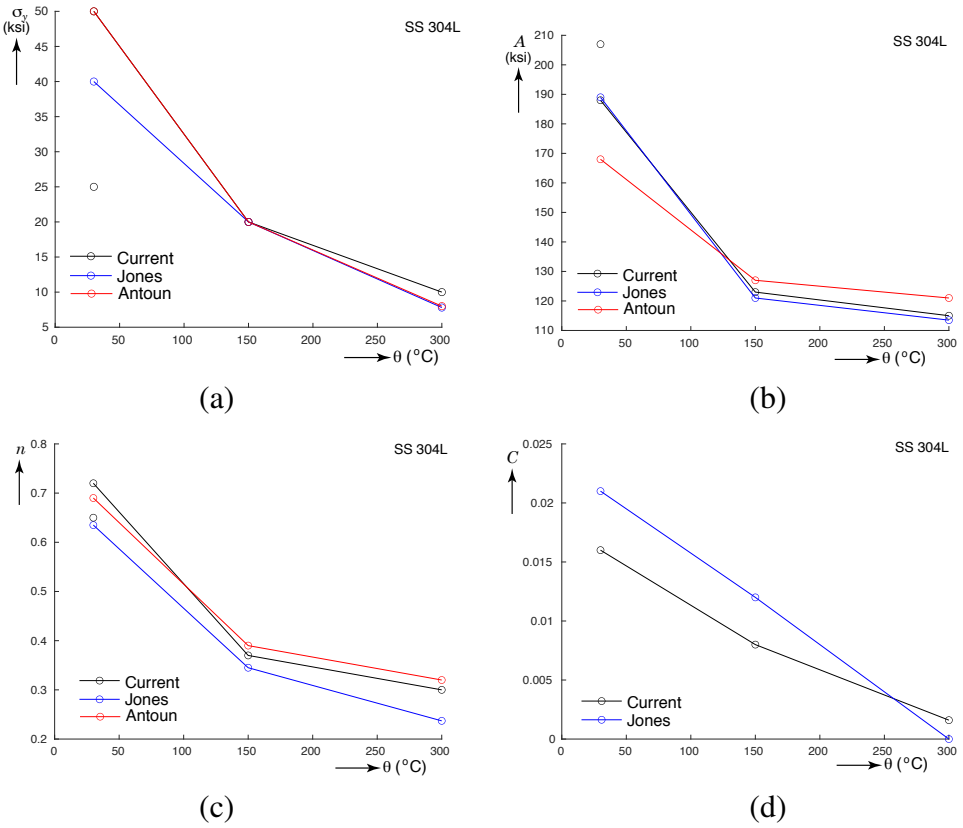

Figure 4-1. Variation of power-law hardening function parameters with temperature for three different lots. (a) σ_y, (b) A, (c) n and (d) C

where $i = 1,2,3$ runs through the three temperatures and $j = 1,2,3,4$ runs across the historical data, the values in the tables plus the added data point mentioned above. Finally, $\bar{\sigma}_y$ is the value of σ_y in the calibration, 42.5 ksi. The bounds for G_A, G_n and G_C are determined in a similar manner.

4.1.3. Variability Results

The results given in Table 4-4 show the lower and upper bounds for each of the four gains, while Fig. 4-2 compares the nominal curves to those that would represent the higher and lower curves based on the gain values in the table. The higher curves correspond to the upper bounds of G_{σ_y} and G_A, but the lower bound of G_n while the lower ones correspond to the opposite choices. These curves were generated for isothermal conditions and a loading rate equal to the reference rate, so G_C did not come into play. Still, the plots give an idea of the range of the material responses that can be achieved by varying the gains within their established range. They appear to be reasonable.

Table 4-4. Lower and Upper bounds for multiplier function gains.

Gain	Lower Bound	Upper Bound
G_{σ_y}	0.588	1.56
G_A	0.894	1.10
G_n	0.790	1.07
G_C	0.458	1.47

4.2. Failure Model

The availability of ductile failure data and calibrations for just about any metal is quite reduced compared to stress-strain data. As a result, a different approach was required. Here, the parameters of the failure model are kept at their nominal values, thus lumping all variability into the value of damage at which material failure is declared. The failure model was calibrated so that the target corresponds to a damage value $D = 1$. The declaration of the value of damage at failure, however, is up to the user. Based on the calibration results, and looking at the curves in Fig. 4-2, a recommended range for the declaration of failure in uncertainty estimations is $0.5 < D < 1.2$. The points in each stress-strain curve shown in Fig. 4-2 that correspond to these bounds have been marked for reference.

4.3. Other Model Parameters

The linearly elastic parameters of the model, Young's modulus and Poisson's ratio, can have some variabilities, but they are generally very small compared to those of other model parameters, even

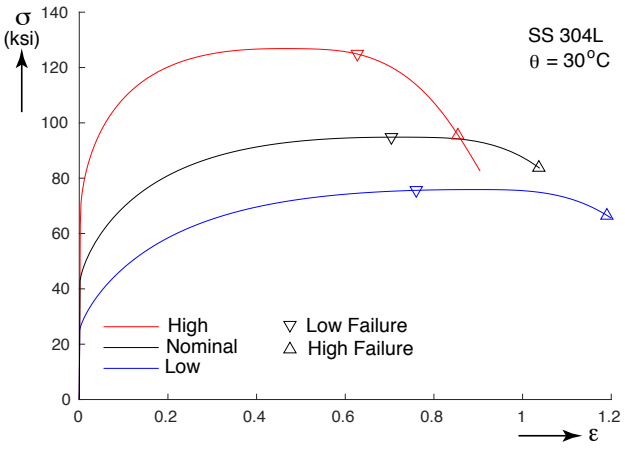

(a)

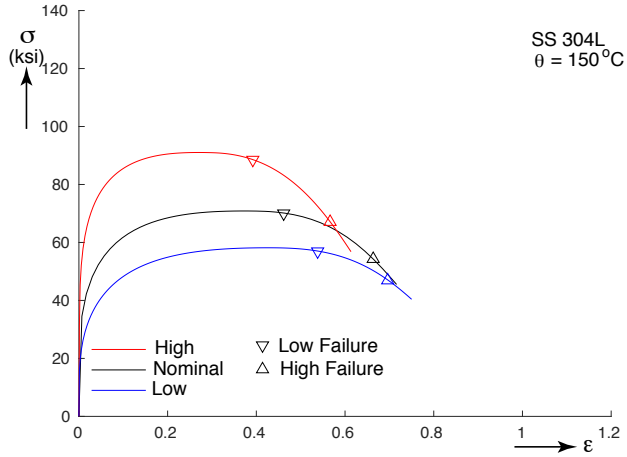

(b)

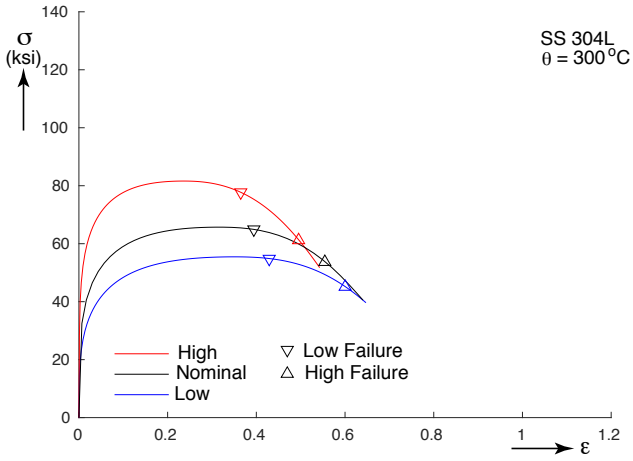

(c)

Figure 4-2. Bounding uniaxial stress-strain curves and corresponding bounds in failure strains.

when comparing across different lots. Since the intent of this model is for calculations that go deep into the plastic range, the variability in the elastic properties can be taken as insignificant.

Variability in the density, ρ is another factor that was not considered in the current work. As with the elastic properties, variations in the material density, even lot-to-lot will be very small since its value is essentially governed by the alloy composition, which is kept within tight bounds (see Table 1-1). Again, for the intended use of this model, the variability in the density can also be neglected.

The density, together with the specific heat capacity, c_p, affect the rise of temperature from plastic work, as indicated in Eq. (3.3). It is recommended that the variability in c_p also be neglected while lumping the uncertainty of the temperature rise in the Taylor-Quinney coefficient β_{TQ}. For ideally isothermal conditions, clearly $\beta_{TQ} = 0$. For adiabatic conditions, it is well known that the value can vary with both strain and strain rate, but the model treats it as a constant. Based on observations made on the effect of this parameter on the shape of the calibrated stress-strain curves, an interval of ± 20 to $\pm 30\%$ seems reasonable. For loading rates that have time scales in the same order as the heat transfer, a coupled thermal and mechanical calculation should be conducted.

5. MODSIM USE OF THE MATERIAL MODEL

The calibrations of the thermal-mechanical, elastic-plastic and ductile failure models for 304L stainless steel presented here are intended to be used in situations where essentially monotonic, large deformations of the material take place relatively fast, with strain rates ranging up to the low thousands per second. The model allows for adiabatic heating due to plastic deformation and remains valid as long as the temperature stays in the range between room temperature and 300°C. The model can also be used in isothermal calculations provided β^{TQ} is set to zero. The experimental data generated covers the environments stated previously and sets the limits of applicability of the model. The experiments used to calibrate the failure model, in particular, span a significant triaxiality range, from about -0.8 to 0.6, so justification exists to use the model for both tensile dominated and shear-dominated states. The calibrated material model is given in Appendix A.

The calibration of the material model was carried out using data from material specimens with length scales in the order of one-tenth of an inch to one inch. This was followed by simulations of the tests using finite element models of the specimens. All simulations used hexahedral elements of the selective deviatoric type that ranged in size from 0.002 to 0.015 in., depending of the specimen being modeled. The use of the material model in structural applications could involve structures with length scales that range from those of the specimens to the order of tens of feet. Since the latter may require use of elements that could be in the order of one inch, a brief look at what could be the effects of element size is warranted.

The number of possible structural geometries is unlimited, but the focus here will be on a simple plate subjected to tension as shown in Fig. 5-1. Two plates with overall dimensions 9 in. by 5 in. and asymmetric notches but similar geometries are shown in Figs. 5-1(a) and (b). In both cases, the thickness is 0.125 in. The difference between them is the root notch radius: blunt with a radius $r = 1.125$ in. or sharp with a radius of $r = 0.5625$ in. The boundary conditions on the plate are in Fig. 5-1(c). The left edge is fully constrained, while the right edge is constrained in two directions and pulled by prescribing the displacement Δ to the right. The notches serve to introduce stress concentrations that accentuate the effect of element size on the response and especially on the failure of the plates.

5.1. Use with Hexahedral Elements

The use of hexahedral elements to discretize the structure is considered first. The elements used remain small as needed to maintain aspect ratios close to one when three or five elements are used through the thickness. The objective is to compare the results obtained with selective deviatoric (SD, with damage reported as the average from the 8 integration points) and mean quadrature

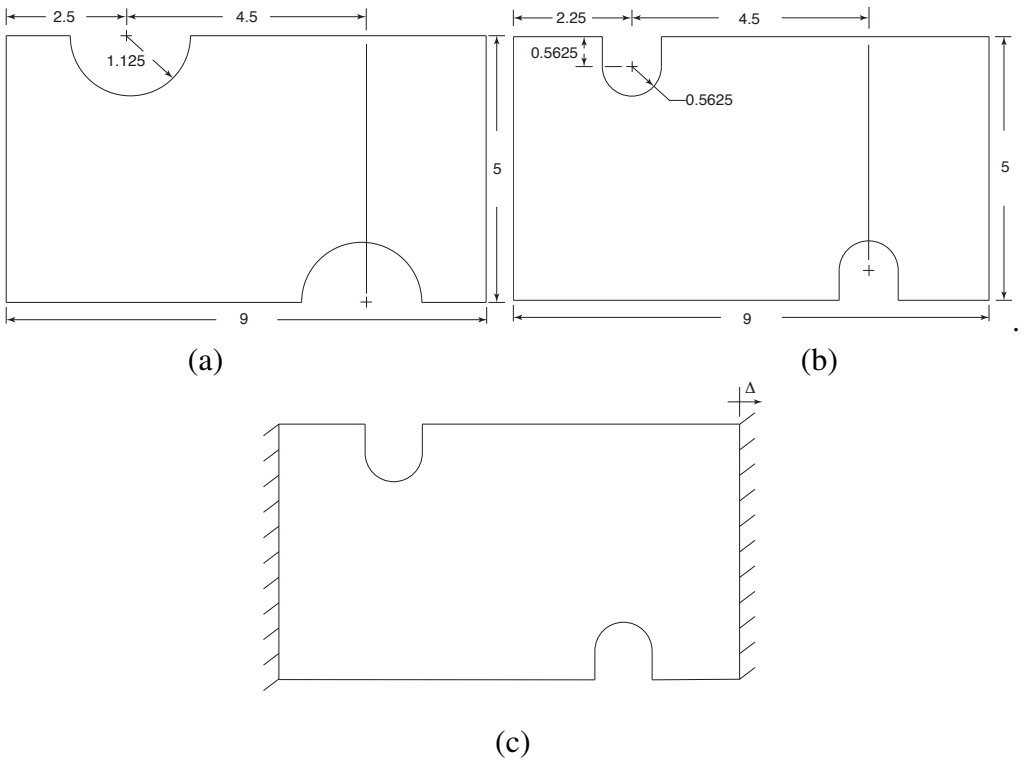

Figure 5-1. Flat plate problem geometry and boundary conditions. (a) $r = 1.125$ **in., (b)** $r = 0.5625$ **in. and (c) boundary conditions.**

(MQ, with damage reported at the single integration point) elements. The hardening rule parameters used in these calculations are those from Table 3-2 at 30°C. Obviously this problem does not excite bending of the plate, so no conclusions will be drawn in that regard.

Figure 5-2(a) shows the calculated load-deflection (F-Δ) response of the plate geometry with $r = 1.125$ in. The responses are essentially identical between the two element types and the two element sizes. Figure 5-2(b) shows the maximum damage D in the model as a function of Δ. Again the accumulation of damage is very similar among all four models. The horizontal dashed line represents $D = 1$, when failure occurs based on the calibration. Taking the case with SD elements of 0.025 in. in size as the benchmark for the rest of the calculations, the vertical dashed line then gives the values of D at which failure should be called in the other cases. The variation is in the order of 10%, which in ductile failure problems could be acceptable, but could be accounted for if desired.

5.2. Use with Shell Elements

Shell elements are generally used to represent structural members whose in-plane dimensions are much larger than their thickness. The advantages of these elements are that significantly fewer of them are required to discretize the structure, therefore reducing the number of degrees of freedom in the model thus making calculations possible for large, plate-like, structures. Larger elements also lead to larger time steps in explicit dynamics simulations, thus reducing the run time of the

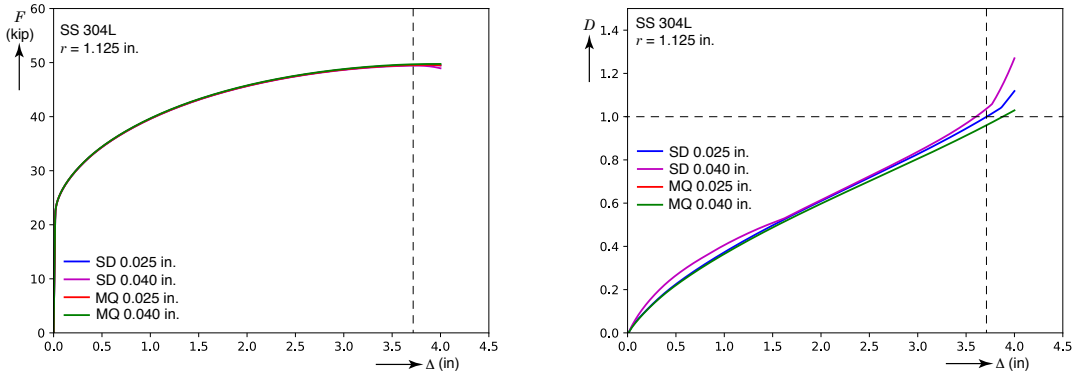

(a) (b)

Figure 5-2. Comparison of predictions with mean quadrature (MQ) elements to selective deviatoric (SD) elements. (a) Force-deflection and (b) Damage-deflection.

analysis. The price to be paid, however, has several components: first, the assumption of plane stress in the element directly affects the evaluation of the mean stress in the calculation of damage, second, they cannot accurately capture necking-like localizations that may precede failure, and third, the larger elements underestimate the values of the stress components, equivalent plastic strain and damage near stress concentrations Still, in many applications it is necessary to estimate when material failure may occur in shell-based models.

Here, the same models in Fig. 5-1 can be used to investigate the performance of shell elements on the calculated response and failure of these plates. As before, the benchmarks for comparisons are the calculation results obtained using selective deviatoric elements with nominal size of 0.025 in. and aspect ratio close to unity in all directions.

Figure 5-3(a) shows the benchmark force-elongation responses, as well as results obtained with Belytschko-Tsai shell elements of sizes 0.25, and 0.5 in. The elements have four nodes and reduced integration with five integration points through the thickness. The meshes are in Figs. 5-3(c) and (d). The effect of the element type and size is relatively small. As expected, the larger element yielded slightly higher loads. The bigger difference can be seen in Fig. 5-3(b) in the plots of maximum damage in the model vs. elongation. Clearly, the shell element models in this case accumulate damage appreciably more slowly than the model with hexahedral elements.

The results for the smaller notch radius, shown in Fig. 5-4 show more pronounced differences between the models with shell and hexahedral elements as well as between the two shell models with different element sizes. Figure 5-4(a) shows bigger differences in the F-Δ responses between the three calculations prior to a displacement of 3 in. Also note that the curve with the hexahedral elements shows a rapidly decreasing load soon afterwards, whereas the shell models do not. The load decrease is due to a thinning instability that developed in the model and that the shell elements did not capture until later, evidenced by the beginning of load decreases at higher displacements. Figure 5-4(b) shows significantly different rates of accumulation of damage between the three cases. Looking at the displacement at which the continuum model reached a

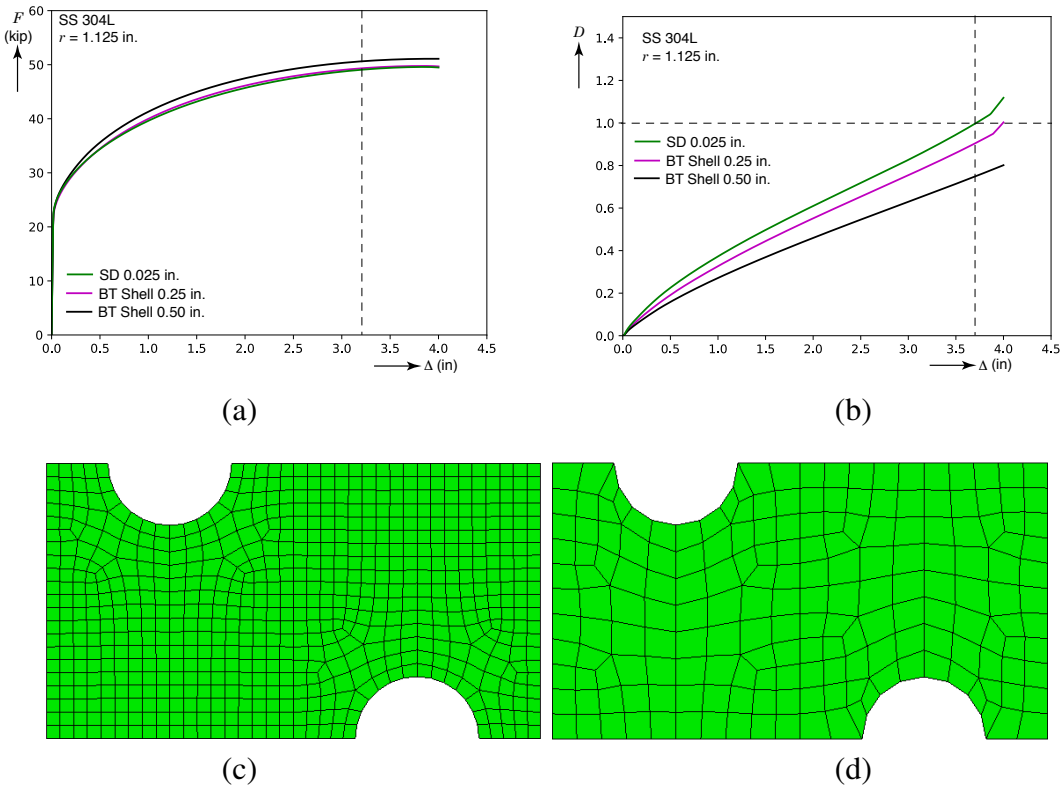

Figure 5-3. Comparison of predictions with Belytschko-Tsai (BT) shell elements to selective deviatoric (SD) elements for a plate with $r = 1.125$ in. notches. (a) Force-deflection, (b) Damage-deflection, (c) mesh with 0.25 in. elements and (d) mesh with 0.5 in. elements.

damage of one, the critical value of damage in the shell models should be set to a lower value. The meshes are shown in Figs. 5-3(c) and (d). Note that as the mesh gets coarser, the details of the distribution of elements around the notch will probably also affect the results.

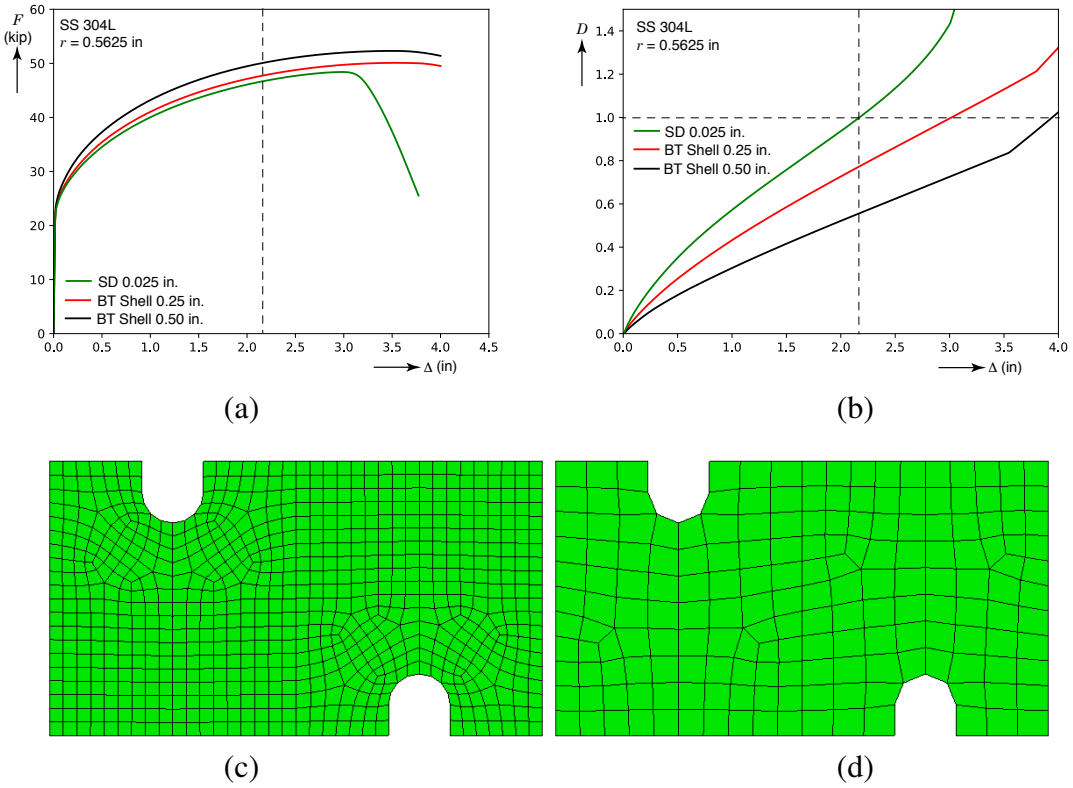

Figure 5-4. Comparison of predictions with Belytschko-Tsai (BT) shell elements to selective deviatoric (SD) elements for a plate with $r = 0.5625$ in. notches. (a) Force-deflection, (b) Damage-deflection, (c) mesh with 0.25 in. elements and (d) mesh with 0.50 in elements.

To address the issue of damage at failure, Figure 5-5(a) plots the variable K, representing the value of the damage D at the displacement at which failure occurred in the model with hexahedral elements, against the element length l. These plots include results for even sharper notches with $r = 0.2813$ in. with the meshes shown in Fig. 5-6. The value of K decreases as l increases, and the values are lower as the notch radius becomes sharper. It seems likely that one way to non-dimensionalize the graph is to plot K against the ratio l/r as has been done in Fig. 5-5(b). Much more work should be conducted to learn if this approach is effective and how it should be applied depending on the loading (tension, bending, torsion), the arrangement of the elements around a given stress concentrator, the material of the part, etc. Note that the lines from each radius do not align perfectly, probably due to the different element arrangements around the notch. The main conclusion is that the value of D used to declare the initiation of failure can strongly depend on the shell element size, and Fig. 5-5 provides some guidance to set the value of D at which the initiation of failure should be declared.

In closing, note that the main factor affecting the results in the plate example above is the

interaction between the element and the stress concentrator. The calculation of hydrostatic stress is not relevant in this case because the failure criterion, based on a constant value of equivalent plastic strain, is independent of the hydrostatic pressure. Also the failure criterion calculated with the hexahedral continuum elements was satisfied prior to the onset of localization, so this issue did not affect the results either.

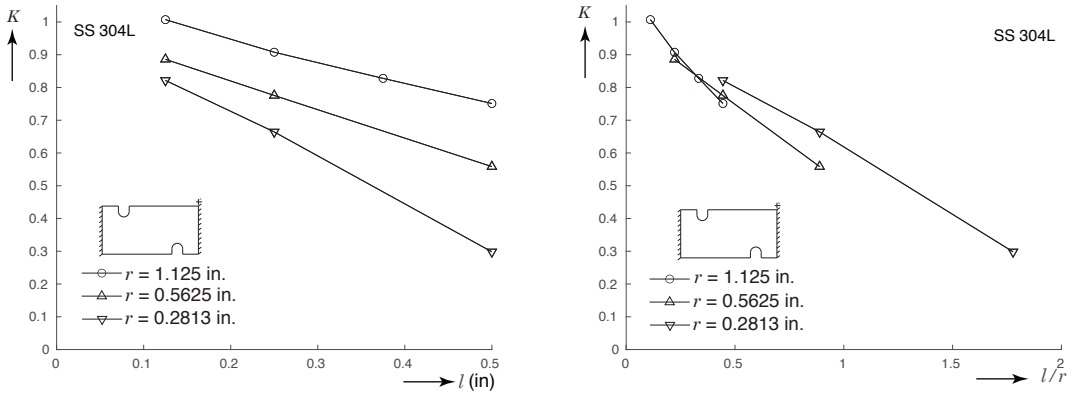

(a) (b)

Figure 5-5. Values of damage at failure, K, as functions of notch radius and element size. (a) As function of element size and (b) as function of normalized element size.

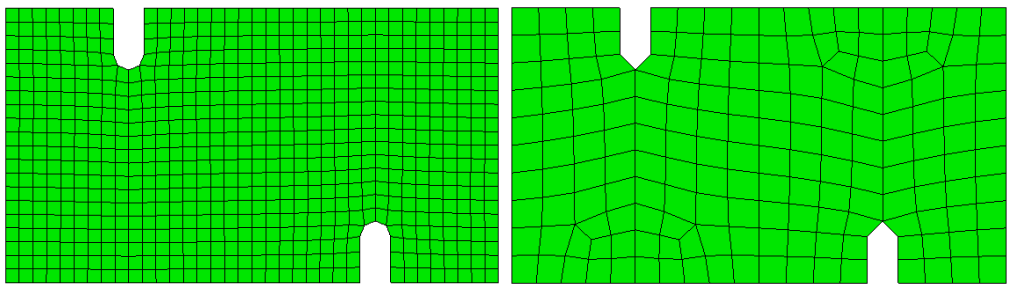

(a) (b)

Figure 5-6. Meshes for geometry with $r = 0.2813$ in. (a) Mesh with 0.25 in. elements and (b) mesh with 0.50 in elements.

The transition between using hexahedral vs. shell elements is likely to occur around the value where the element size is about the thickness of the plate. In this respect, Table 5-1 compares the values of K for both types of elements with size of 0.125 in. For each case considered, the differences are small, with the shell elements having slightly smaller values and the values for both elements decreasing with decreasing notch radius.

Table 5-1. Comparison of values of K for selective deviatoric hexahedral elements and BT shell elements of size 0.125 in.

r, in	SD-Hex	BT-Shell
1.125	1.037	1.007
0.5625	0.9157	0.8886
0.2813	0.8655	0.8215

REFERENCES

[1] Sierra Solid Mechanics Team. Sierra/SolidMechanics 4.58 user's guide, Sandia Technical Report SAND2020-10045, September, 2020.

[2] Wikipedia. Stainless steel. en.wikipedia.org.

[3] ASM Aerospace Specification Metals Inc. *asm.mateweb.com*

[4] Gearhart, J. and Silver, S. Pallet assembly material characterization. Memo to J. Arnold, April, 2019.

[5] Sanborn, B. and Song, B. High strain rate tension testing of 304L and 6061-T6. Memo to distribution, May, 2020.

[6] Song, B. Dropkinson Bar for Intermediate strain-rate testing – design, development, verification, and application. Sandia technical report SAND2017-9393, August 2017.

[7] Corona, E., Deibler, L.A., Reedlunn, B., Ingraham, M.D. and Williams, S. An experimenal study of shear-dominated failure in the 2013 Sandia Fracture Challenge specimen. Sandia technical report SAND2015-2850, 2015.

[8] Corona, E. Shear-dominated failure in the 'hat' specimen from the 2013 Sandia Fracture Challenge. Memo to B. Reedlunn, SAND2016-11740R, September, 2016.

[9] Corona, E. and Lester, B. V&V of thermal-mechanical failure – FY2017: failure of a laser-welded pressurized container. Memo to distribution, SAND2017-11141R.

[10] de Almeida, L.H., Le May, I. and Emygdio, P.R.O. Mechanistic modeling of dynamic strain aging in austenitic stainless steels, *Materials Characterization*, V. 41, pp. 137–150, 1998.

[11] Corona, E., Jones, A. and Rees, J. FY18 thermal mechanical failure: SS-304L calibration, Taylor-Quinney parameter measurement and kinematic hardening plastlcity. Memo to distribution, SAND2018-14318R, December, 2018.

[12] Johnson G.R. and Cook, W.H. Fracture characteristics of three metals subjected to various strains, strain rates, temperatures and pressures, *Engineering Fracture Mechanics*, V. 21, pp. 31–48, 1985.

[13] Communication with Brian Lester, 2020.

[14] LAMÉ Team. Library of Advanced Materials for Engineering (LAMÉ) 4.58. Sandia Technical Report SAND2020-10268, 2020.

[15] Lester, B.T. and Scherzinger, W.M. Modular plane stress plasticity material model. Memo to distribution, SAND2019-3151R, March, 2019

[16] Lester, B.T. and Scherzinger, W.M. Adiabatic heating in modular plasticity models. Memo to distribution, SAND2019-15003R, December 2019.

[17] Lester, B.T. and Scherzinger, W.M. Failure formulations in modular plasticity models. Memo to distribution, SAND2019-9867R, August, 2019.

[18] Jones, A., Jones, E., Reedlunn, B. and Kramer, S. Conversion of plastic work to heat: a full-field study of thermomechanical coupling, Sandia Technical Report SAND2018-10763, 2018.

[19] VanGoethem, D. Plate tear out test and model comparisons. Communication on January, 2020.

[20] Communication with B. Antoun, 2015.

[21] Shand, L. Moore, L and Wilson,L. Memo to A. Brink, Dec. 2020.

[22] Fietek C. Analysis of element size and element type on material model performance. Memo to distribution. December 2020.

APPENDIX A. Sierra Input for the Calibrated Model

```
#  Material calibration for 304L Stainless steel
#  Units: Mechanical - lb/in/s, Thermal - Celsius
#  Material model: j2_plasticity
#  Material sub-model: power-law-parameter
#  Adiabatic or Isothermal response set by the parameter beta_tq.  0.5 for
#  adiabatic and 0.0 for isothermal
#  Temperature dependency of the plasticity and failure models are
#   given using xy functions.
#  Strain rate dependence is Johnson-Cook with a temperature-dependent parameter
#
#  Modular failure model: Wilkins with alpha=beta=0, which corresponds to an
#   equivalent plastic strain to failure
#
#  User guide:
#  1. VARIABLES DEFINED IN THIS FILE:The variables matl and modl are provided
#     for a more convenient interface with a Sierra/SM input file.
#     matl = 'ss304l_plp' and modl = 'j2_plasticity'
#
#  2. THERMAL SENSITIVITY STUDIES: The tabular functions for the plasticity
#     model parameters can be varied
#     by prescribing a y scale in each function.  The recommended ranges for
#     sensitivity studies are:
#     ================================================================================
#     Parameter            Minimum y scale     Maximum y scale      Variable name
#     --------------------------------------------------------------------------------
#     yield stress               0.5882            1.565           yield_stress_scale
#     hardening constant         0.8936            1.101           hardening_constant_scale
#     hardening exponent         0.7902            1.066           hardening_exponent_scale
#     rate constant              0.4580            1.466           rate_constant_scale
#     ================================================================================
#     Placeholders for the y scales are included in each function
#     Define the variables in the Sierra/SM input according to the variable names in the table.
#     These variables must be defined.  For the nominal calibration set all to 1.0
#
#  3. THERMAL CONDITION: A string variable named thermal_state must be defined to set the
#     thermal condition.  Set thermal_state = 'isothermal' for an isothermal analysis, or to
#     'adiabatic' for an adiabatic analysis.  Any other string will result in an error.
#
#  4. INITIAL TEMPERATURE: An initial condition block must be included to define the initial
#     temperature.  The model has been calibrated between 30 and 300 C.
#
#  5. RATE DEPENDENCY: The material model is rate-dependent.  Make sure that the structural
#     model is loaded at the correct rate.  The failure model is also rate-dependent.
#
#  6. FAILURE MODEL: The failure model produces an output variable damage.
#     It is calibrated so when damage=1 the material fails for
#     the nominal calibration.   The recommended range for sensitivty
#     studies of the damage is from 0.5 to 1.2.  There are no changes to be made in this file,
#     instead, inspect the output to determine the range of failure, or in an element death
#     block declare the value of damage at which an element will be killed.  The model
#     calibration is intended for failure initiation.  It does not include any failure
#     propagation information.
#
#
#{matl = 'ss304l_plp'}
#{modl = 'j2_plasticity'}
begin property specification for material ss304l_plp
```

```
  density = 7.49e-4
  begin parameters for model j2_plasticity
    youngs modulus = 28.e6
    poissons ratio = 0.27
    yield stress = 42.5e3
            hardening model = flow_stress_parameter
            isotropic hardening model = power_law_parameter
            hardening constant = 188.e3
            hardening exponent = 0.72

            rate multiplier = johnson_cook_parameter
            rate constant = 0.016
            reference rate = 3.33e-4


            yield stress function       = da304YieldStressFunction
            hardening constant function = da304HardConFunction
            hardening exponent function = da304HardExpFunction
            rate constant function      = da304RateConFunction

            thermal softening model = adiabatic
            specific heat = 0.776e6
    #{beta1= (thermal_state == 'isothermal' ? 0.0 : 5)}
    #{beta2 =  (thermal_state == 'adiabatic' ? 0.5 : 5)}
            #{beta3 = min(beta1,beta2)}
            #{beta = (beta3 == 5 ? -1.e50 : beta3)}
    beta_tq = {beta}
            t0 = 30.

            failure model = modular_failure
              critical failure parameter = 1.13
              pressure multiplier = wilkins
                wilkins alpha = 0.
                wilkins pressure = 300.e3
              lode angle multiplier = wilkins
                wilkins beta = 0.000
              rate fail multiplier = user_defined
               rate fail multiplier function = da304FailureRateFunction
              temperature fail multiplier = user_defined
                temperature fail multiplier function = da304FailureTemperatureFunction


  end parameters for model j2_plasticity
end property specification for material ss304l_plp


        begin function da304YieldStressFunction
          type is piecewise linear
  y scale = {yield_stress_scale}
          begin values
            30. 1.0
            150. {20./50}
            300. {10./50.}
            1400. {0./50.}
           end values
        end function da304YieldStressFunction

        begin function da304HardConFunction
          type is piecewise linear
  y scale = {hardening_constant_scale}
          begin values
            30. 1.0
            150. {123.16/188.}
            300. {115./188.}
            1400. {0./188.}
          end values
        end function da304HardConFunction
```

```
      begin function da304HardExpFunction
        type is piecewise linear
y scale = {hardening_exponent_scale}
        begin values
          30. 1.0
          150. {0.3717/0.72}
          300. {0.3/0.72}
          1400. {0./0.72}
        end values
      end function da304HardExpFunction

      begin function da304RateConFunction
        type is piecewise linear
y scale = {rate_constant_scale}
        begin values
          30. 1.0
          120. 1.0
          150. 0.50
          300. 0.10
  1400. 0.0 # Not measured, but extrapolated
        end values
      end function da304RateConFunction

      begin function da304FailureRateFunction
        type is piecewise linear
        begin values
          3.33e-4 1.
           0.1    1.40
          217.    1.25
          1500.   1.25
          3500.   1.25
        end values
      end function da304FailureRateFunction

      begin function da304FailureTemperatureFunction
        type is piecewise linear
        begin values
          30. 1.0
         150. 1.27
         300. 1.34
       end values
      end function da304FailureTemperatureFunction
```

DISTRIBUTION

Email—Internal

Name	Org.	Sandia Email Address
Technical Library	1911	sanddocs@sandia.gov

E. Jones	1512
D. Farrow	1528
B. Song	1528
B. Schroeder	1544
P. Grimmer	1554
D. VanGoethem	1554
J. Bishop	1556
J. Mersch	1556
D. Najera-Flores	1556
E. Fang	1558
K. Johnson	1558
N. Reedlunn	1558
W. Scherzinger	1558
A. Brink	6621
J. Ostien	8363
B. Talamini	8363
S. Nelson	8750
L. Beghini	8752
K. Karlson	8752
A. Stershic	8752

Sandia National Laboratories

Sandia National Laboratories is a multimission laboratory managed and operated by National Technology & Engineering Solutions of Sandia LLC, a wholly owned subsidiary of Honeywell International Inc., for the U.S. Department of Energy's National Nuclear Security Administration under contract DE-NA0003525.